



An experimental investigation on R245fa and R1233zd(E) flow boiling at high saturation temperatures in a horizontal small diameter channel

D.B. Marchetto ^{a,*}, R. Revellin ^b, R. Rullière ^b, G. Ribatski ^a

^a Heat Transfer Research Group, São Carlos School of Engineering – University of São Paulo, São Carlos, SP, Brazil

^b Univ de Lyon, INSA Lyon, CNRS, CETHIL, UMR5008, Villeurbanne 69621, France



ARTICLE INFO

Keywords:

Flow boiling
Heat transfer
Pressure drop
High-temperature
Microchannel
Organic Rankine cycle

ABSTRACT

The current study presents an investigation on flow patterns, pressure-drop and heat transfer coefficient for the refrigerants R1233zd(E) and R245fa flowing at saturation temperatures (T_{sat}) between 75 °C and 95 °C inside a horizontal 2 mm diameter tube. Experimental results are reported for mass velocities of 176–570 kg/m²s and heat fluxes of 18.1–54.5 kW/m². As expected, the pressure gradient increases as the mass velocity increases and the saturation temperature decreases. Flow image analysis indicated that the pressure gradient peak is associated with disturbance interfacial waves damping. Heat transfer coefficient data indicated strong contribution of nucleate boiling effects for most of the experimental conditions. The higher the saturation temperature and the heat flux, the higher the heat transfer coefficient, regardless of the vapor quality range. In general, the effect of mass velocity on the heat transfer coefficient was only marginal, with exception of low T_{sat} and heat flux conditions. Two of 20 pressure-drop prediction methods predicted more than 90% of the database within error bands of ±30%. Overestimation of heat transfer coefficient data was verified for most of the 16 evaluated prediction methods, especially at high T_{sat} . Only two methods predicted more than 80% of data within an error band of ±30%.

1. Introduction

Economic and technological developments over the past centuries have been accompanied by a sharp growth in energy consumption. Burning fossil fuels was, and still is, the main primary energy source for power generation [1]. However, the progressive depletion of fossil fuels [2] motivated the development of high efficiency thermal systems, as well as alternatives for reusing the residual heat generated during their combustion. In addition, fossil energy combustion is usually pointed out as the main cause of global climate change, which resulted in several laws and international standards to control the use of these resources, accelerating their replacement by renewable sources, such as: geothermal, biomass and solar energy [2].

Due to its simple structure, high reliability, low cost and easy maintenance, the Organic Rankine Cycle (ORC) is one of the most promising technologies for power generation using low-grade heat sources and waste heat [3–5]. The ORC structure is similar to that of traditional Rankine cycles, but using organic working fluids, instead of water. The reduced critical temperature (T_{crit}) of these fluids, in

comparison with water, allow the use of almost any low-to-medium temperature heat sources [3]. Another technology that has been subject of interest recently is the high temperature heat pump (HTHP). Using a small amount of electrical energy, heat pumps extract heat from a lower temperature source, and provide it at a higher temperature level. Outdoor air, ground heat or ground water are typical heat sources for traditional heat pumps, however, with the increase of the operating temperatures, the HTHPs are allowed to reuse waste heat from industrial processes [6]. A promising application of the HTHPs is to provide a heat source for boilers, replacing the fossil fuels burning process [7]. The combination of both ORC and HTHP have also been studied as a concept of energy storage known as Carnot Battery. In this approach, the heat output of the HTHP can be directly used, or stored over several hours up to a few days, and applied as a heat source to generate electrical energy through the ORC when necessary [8].

According to Zhang et al. [9], heat sources typically used in ORCs operate at temperatures between 100 and 250 °C, which results in evaporating temperatures of 50–150 °C. Considering the refrigerant R245fa, which is frequently pointed out as a high-performance fluid in ORCs systems [10–12], these saturation temperatures correspond to

* Corresponding author.

E-mail address: daniel.marchetto@usp.br (D.B. Marchetto).

| Nomenclature | | <i>adiabatic</i> | Adiabatic |
|-----------------------|--|----------------------|--|
| <i>c_p</i> | Specific heat capacity J/kgK | <i>amb</i> | Ambient |
| <i>D</i> | Diameter m | <i>bottom</i> | Bottom |
| <i>G</i> | Mass velocity kg/m ² s | <i>crit</i> | Critical |
| <i>h</i> | Heat transfer coefficient W/m ² K | Δp | Related to pressure drop |
| <i>I</i> | Electrical current A | <i>eff</i> | Effective |
| <i>i</i> | Specific enthalpy J/kg | <i>el</i> | Electrical |
| <i>i_{lv}</i> | Enthalpy of vaporization J/kg | <i>f</i> | Frictional |
| <i>k</i> | Thermal conductivity W/mK | <i>fluid</i> | Working fluid |
| <i>L</i> | Length m | <i>H</i> | Hydraulic |
| <i>p</i> | Pressure Pa | <i>h</i> | Heated |
| <i>p_r</i> | Reduced pressure [-] | <i>i</i> | Internal |
| Δp | Pressure drop Pa | <i>in</i> | Inlet |
| <i>M</i> | Molar mass kg/kmol | <i>l</i> | Liquid |
| \dot{m} | Mass flow rate kg/s | <i>loss</i> | Losses |
| \dot{q} | Volumetric heat generation VW/m ³ | <i>meas</i> | Measured |
| \dot{Q} | Heat transfer rate W | <i>middle</i> | Middle |
| q'' | Heat flux W/m ² | <i>o</i> | Outer |
| <i>T</i> | Temperature °C | <i>out</i> | Outlet |
| <i>U</i> | Electrical voltage V | pH | Preheater |
| <i>x</i> | Vapor quality [-] | <i>sat</i> | Saturation |
| <i>z</i> | Flow Direction m | <i>top</i> | Top |
| <i>Greek letters</i> | | <i>TS</i> | Test section |
| α | Void fraction [-] | <i>v</i> | Vapor |
| ΔT_{wall} | Wall temperature difference °C | <i>wi</i> | Internal wall surface |
| $\lambda_{30\%}$ | Fraction of data predicted within error bands of 30% [-] | <i>wo</i> | Outer wall surface |
| μ | Viscosity Pa.s | Abbreviations | |
| η_{loss} | Relative heat losses [-] | GWP | Global warming potential |
| ρ | Density kg/m ³ | HTC | Heat transfer coefficient |
| σ | Surface tension N/m | HTHP | High temperature heat pump |
| Subscripts | | MAE | Mean absolute error, $MAE = \frac{1}{N} \sum \epsilon $ |
| <i>1φ</i> | Single-phase | ORC | Organic Rankine cycle |
| <i>accel</i> | Accelerational | VHTHP | Very high temperature heat pump |

Table 1
Experimental studies for organic refrigerants at saturation temperatures higher than 50 °C.

| Authors | Geometry | <i>D_H</i> [mm] | Fluids (<i>T_{sat}</i> [°C]) | <i>G</i> [kg/m ² s] | <i>q''</i> [kW/m ²] | Measurement |
|---|------------------|---------------------------|---|--------------------------------|---------------------------------|-----------------|
| Zhang and Webb [14] | C single/multi H | 2.13–6.20 | R134a (40–65), R22 (25–50), R404A (28–42) | 400–1000 | 0 | Δp |
| Vassallo and Keller [15] | R single V | 4.8 | R134a (35.5–75.8) | 510–2040 | 0 | Δp |
| Vijayarangan et al. [16] | C single V | 12.7 | R134a (39.4–97.8) | 1200–2000 | 35–80 | Δp |
| Costa-Patry et al. [17] | R multi H | 0.25 | R245fa (30–51), R134a (30–51), R1234ze (30–51) | 205–570 | 19–403 | HTC, Δp |
| Charnay et al. [18–21] | C single H | 3 | R245fa (60–120) | 100–1500 | 0–90 | HTC, Δp |
| Mawatari and Mori [22] | C single V | 4.4 | R134a (99.1–100.6), R22 (94.7–95.7) | 400–1000 | 9–46 | HTC |
| Billiet et al. [23] | C single H | 3 | R245fa (40–125) | 100–1000 | 10–54 | HTC |
| Layssac et al. [24,25] | C single H/V/I | 1.6 | R245fa (81) | 100–300 | 0–13.5 | HTC, Δp |
| Zhang et al. [9] | C single H | 10.3 | R134a (21.6–90.8) | 300–600 | 20–50 | HTC |
| Lillo et al. [26] | C single H | 6 | R1233zd(E) (25–65) | 150–300 | 2.4–41 | HTC |
| Wang et al. [27] | C single H | 10 | R245fa (40–60) | 193–386 | 10–36* | HTC |
| Guo et al. [28] | C single H | 10 | R245fa (55–95), R134a (10–85), R134a/R245fa (75–95) | 100–300 | 6–24 | HTC, Δp |
| Zhao et al. [29] | C single V | 4 | R245fa (36.6), R1233zd(E) (40.4–68.6), R1224yd(Z) (34.2–53.1), HFE347pcf (70) | 20–40 | 6–20 | HTC |
| You et al. [30] | R multi H | 1.2 | R1233zd(E) (38–56) | 100–450 | – | HTC |
| Arcasi et al. [31] | C single H | 6 | R1233zd(E) (25–65), R448A(25–55), R452A (25–45), R455A (25–55) | 150–600 | 0 | Δp |
| Halon et al. [32] | R multi H | 1 | R245fa (49–82) | 400–1000 | 30–50 | HTC |
| Kaya et al. [33] | C single H | 21 | R245fa (85–120) | 83–286 | 17–29 | HTC |
| Li and Hrnjak [34] | R multi H | 0.64 | R1233zd(E) (30–50), R1336mzz(Z) (40–60) | 100–200 | 0–6 | HTC, Δp |
| Luo et al. [35] | C single H | 10 | R245fa (80–115) | 248–460 | – | HTC |
| Pysz et al. [36], Pysz and Mikielewicz [37] | C single V | 2–3 | R1233zd(E) (83–145) | 200–1000 | 20–43 | HTC, Δp |

C: Circular; R: Rectangular; H: Horizontal; I: Inclined; V: Vertical.

reduced pressures (p_r) ranging from 0.09 to 0.93. According to Arpagaus et al. [6], HTHPs heat source temperatures are higher than 40 °C, but they can reach 120 °C in the so-called very-high temperature heat pumps (VHTHPs).

Vapor-phase density and viscosity (ρ_v , μ_v) increase with increasing reduced pressure, while the liquid density and viscosity (ρ_l , μ_l) reduce. Non-linear behaviors are verified for ρ_l and ρ_v near the critical point ($p_r \approx 0.8$). The progressive convergence of ρ_l and ρ_v , and μ_l and μ_v , are also verified, until they become equal at $p_r = 1$. Enthalpy of vaporization and surface tension reduce with increasing p_r , while the liquid specific heat presents a slight increase followed by a sharp increment close to $p_r = 1$. These changes in thermophysical properties considerably affect the flow and heat transfer behaviors, diverging from those typically verified at low p_r . Since most of the prediction methods currently available in literature were developed for refrigeration and air conditioning applications, i.e. low saturation temperatures and pressures (T_{sat} and p_{sat}), their loss of accuracy can be expected at high p_r [13].

Heat transfer coefficient (HTC) and pressure drop (Δp) are key parameters in the design and optimization of evaporators for thermal systems, therefore their accurate prediction is indispensable for a reliable and optimized project. Although the number of publications involving ORCs and HTHPs has rapidly grown in recent years, flow boiling studies in the T_{sat} range of these applications are still scarce, making it difficult to guarantee the validity of the available prediction methods. Table 1 summarizes flow boiling heat transfer and pressure drop investigations found in the literature for $T_{sat} \geq 50^\circ\text{C}$, indicating the corresponding operating conditions evaluated.

Most of the studies presented in Table 1 were published in the last five years, indicating the current relevance of the subject. In addition, R245fa is the working fluid that predominated in the studies summarized in Table 1, reinforcing its potential of application in ORCs and HTHPs. Due to the agreements and regulations about replacing traditional refrigerants by eco-friendly ones, the number of flow boiling studies using low global warming potential (GWP) refrigerants has grown in recent years, and this trend is also verified for high-temperature investigations, as indicated in Table 1. Several investigations conducted in plate heat exchangers are also found in the literature [38–40], but were not included in Table 1, since they are outside the scope of the present study.

Among the pressure drop studies summarized in Table 1, only six of them [14,15,19,24,31,34] presented results obtained during adiabatic flow, for which the evaluation of the frictional parcel of the pressure gradient is recognized easier. The experimental behavior and the operational parameter effects reported in these studies were similar to those verified at low temperatures and pressures, as pointed out by Marchetto et al. [13]. Comparisons between experimental data and frictional pressure gradient prediction methods are also found in these studies.

Zhang and Webb [14] verified that the prediction method of Friedel [41] presented loss of accuracy as the saturation pressure increases. Based on their experimental data, the authors modified this method, explicitly including p_r effect, obtaining a mean absolute error (MAE) of 11.5 % and 85 % of the data predicted within ± 30 % error band. Vassallo and Keller [15] compared their experimental results obtained for a high aspect ratio rectangular channel with 5 prediction methods, and Chisholm [42] was the most accurate, although its progressive loss of accuracy was verified with increasing T_{sat} . Charnay et al. [19] compared the accuracy of an extensive list of 23 prediction methods, and the empirical correlation of Müller-Steinhagen and Heck [43] was the most accurate, predicting 75.9% of their R245fa data at 60–120 °C within ± 30 % error band, and obtaining a MAE of 24.9 %. Later, Layssac et al. [24] evaluated the effect of the channel orientation on the pressure drop of R245fa flowing in a sapphire ITO-coated tube with an inner diameter of 1.6 mm. The prediction method of Beggs and Brill [44] presented the lowest MAE for predicting their data, and all the 23 methods evaluated by them showed lower accuracy for downward flow

Table 2
Properties of the fluids evaluated in the present study [54].

| Properties | R245fa | | R1233zd(E) | |
|-------------------------------|----------------------|----------------------|----------------------|----------------------|
| | 75 °C | 95 °C | 75 °C | 95 °C |
| p_r [-] | 0.190 | 0.309 | 0.160 | 0.258 |
| ρ_l [kg/m ³] | 1187.9 | 1114.2 | 1129.9 | 1066.9 |
| ρ_v [kg/m ³] | 38.295 | 63.898 | 30.692 | 50.004 |
| μ_l [Pa.s] | 0.000214 | 0.000166 | 0.000177 | 0.000144 |
| μ_v [Pa.s] | $1.23 \cdot 10^{-5}$ | $1.31 \cdot 10^{-5}$ | $1.21 \cdot 10^{-5}$ | $1.28 \cdot 10^{-5}$ |
| k_l [W/mK] | 0.072142 | 0.065965 | 0.068399 | 0.063107 |
| k_v [W/mK] | 0.01721 | 0.019394 | 0.015045 | 0.01704 |
| $c_{p,l}$ [kJ/kgK] | 1.4675 | 1.5633 | 1.3216 | 1.39 |
| $c_{p,v}$ [kJ/kgK] | 1.1 | 1.2308 | 0.98218 | 1.077 |
| i_v [kJ/kg] | 157.92 | 140.53 | 161.39 | 146.42 |
| σ [N/m] | 0.007456 | 0.005185 | 0.008342 | 0.006087 |
| M [kg/kmol] | | 134.05 | | 130.5 |
| GWP | | 1030 | | 1 |

data. This was expected, since the effect of the inclination was more pronounced under downward slopes, and most of the methods do not consider data under these conditions in their development. The frictional pressure drop of three low global warming potential (GWP) refrigerants at saturation temperatures between 25 and 65 °C was evaluated by Arcasi et al. [31]. The authors reported that, at the same experimental conditions, the pressure drops of the evaluated low-GWP mixtures (R448A, R452A and R455A) were considerably closer, while the results obtained for R1233zd(E) reached values 560 % higher, which is associated with the higher vapor-to-liquid density ratio of this fluid. The method of Friedel [41] was the most accurate in predicting the data of Arcasi et al. [31], with more than 73 % of the database predicted within error bands of ± 30 %. Li and Hrnjak [34] also investigated the pressure drop of low GWP refrigerants, but in a 24-port microchannel tube with average hydraulic diameters of 0.643 mm. According to Li and Hrnjak [34], the prediction method of Hwang and Kim [45], proposed for microchannels (0.244–0.729 mm), presented the lowest MAE in predicting their data, 14.1 % and 16.7 % for R1233zd(E) and R1336mzz (Z), respectively.

The heat transfer studies summarized in Table 1 reported different behaviors for the HTC as a function of vapor quality (x). The following trends were the most identified: (i) invariability of the HTC; (ii) increasing HTC with x increment; (iii) decreasing HTC with increasing x ; and (iv) decreasing HTC at low vapor qualities, followed by HTC increase at intermediate and high x . The occurrence of these behaviors is strongly related to the dominance of nucleate boiling and convective heat transfer mechanisms, which are consequence of the reduced pressure, mass velocity (G) and heat flux (q') effects, as well as the channel dimension and geometry. An extensive review about the heat transfer behaviors and the associated mechanisms is presented by Marchetto et al. [13].

In general, the studies reported that the increase of q' and p_r imply on the increase of the heat transfer coefficient, especially when nucleate boiling is the predominant heat transfer mechanism. Under the dominance of convective effects, the higher the mass velocity, the higher the HTC is. However, under the dominance of nucleate boiling effects, increasing the mass velocity may either reduce the heat transfer coefficient or have no effect. However, divergences from these general trends and behaviors described are also reported in the literature. In addition, as pointed out by Marchetto et al. [13], data reported by independent studies at similar high p_r experimental conditions present strong divergences, e.g. HTC results obtained by Zhang et al. [9] and Guo et al. [28] at almost similar working conditions presented differences higher than 350 %.

The difficulty of accurately predicting the heat transfer coefficient at high p_r was reported in several studies summarized in Table 2. Charnay et al. [21] compared their experimental results for R245fa at 60–120 °C with 26 pre-dryout prediction methods, and a general trend of

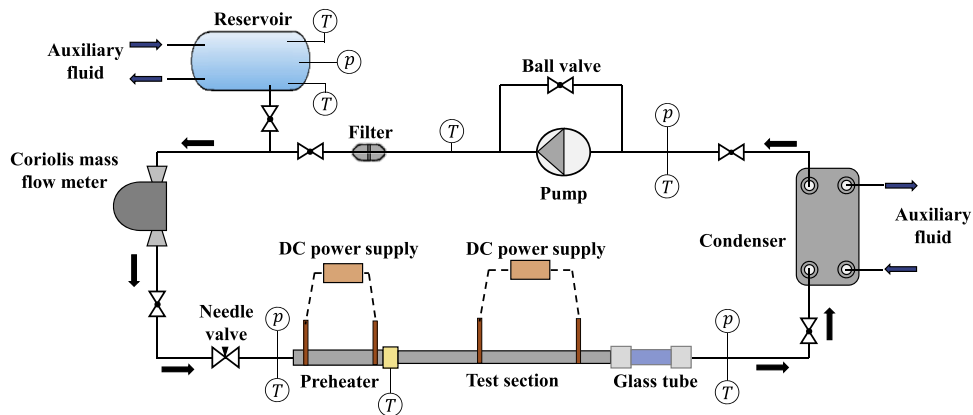


Fig. 1. Schematic view of the experimental facility.

underestimation was verified. Underestimated predictions were also reported by Lillo *et al.* [26] and Pysz *et al.* [36], for all methods evaluated by these authors. Charnay *et al.* [21] reported a reasonable agreement between their data and the method of Choi *et al.* [46], which was proposed for CO₂ flow boiling in small diameter channels (1.5–3 mm). The low critical temperature of CO₂ results in high p_r flow boiling even under T_{sat} conditions typical of refrigeration. Such a fact may justify the accuracy of methods proposed for this fluid when predicting high T_{sat} data of organic refrigerants. Later, Billiet *et al.* [23] extended the database of Charnay *et al.* [21] adding R245fa experimental data at $T_{sat}=40$ °C and 125 °C and included a flow pattern dependency in the correlation of Choi *et al.* [46], reducing its MAE in 11.7%. On the other hand, the method of Choi *et al.* [46] did not provide satisfactory predictions of the recent experimental results obtained by Halon *et al.* [32] also for R245fa (49–82 °C). According to Halon *et al.* [32], the lowest MAEs were provided by the methods of Tran *et al.* [47], 23.7%, Thiangtham *et al.* [48], 23.7%, and Bertsch *et al.* [49], 25.1 %, even though these methods were developed based on data for low temperature and pressures ($p_r < 0.2$). Layssac *et al.* [25] also pointed out the accuracy of the method of Bertsch [49], predicting 80% of their experimental data for a 1.6 mm channel under different inclinations within $\pm 30\%$ error band. Other methods, as those proposed by Gungor and Winterton [50] and Liu and Winterton [51] also presented reasonable accuracy for some datasets [28,29,34,35].

Based on the aspects previously described, it is evident that there is no agreement between the accuracy of the available prediction methods when applied at high T_{sat} flow boiling conditions. Although some authors [23,26,27–29,35], based on their own experimental results, have recently developed prediction methods, their accuracy still need to be confirmed for high T_{sat} independent databases. In summary, the lack of experimental data and the divergences among experimental results

obtained under similar conditions verified in literature is still a limitation to the development of accurate design tools for ORCs and HTHPs. In this context, the present study aims to contribute to filling these gaps by presenting new experimental data for flow boiling of refrigerants R1233zd(E) and R245fa at saturation temperatures between 75 °C and 95 °C inside a horizontal stainless-steel tube with an internal diameter of 2 mm. Adiabatic frictional pressure gradient and heat transfer coefficient data are reported for mass velocities varying from 185 to 560 kg/m²s. The accuracy of well-known and recently developed prediction methods from literature is investigated, focusing on the effect of the saturation temperature on their accuracy. The present study also presents a flow pattern evaluation, in order to investigate the T_{sat} effect on the flow topology and how it affects the pressure drop and heat transfer.

2. Experimental apparatus

The test bench, previously employed by Charnay *et al.* [18–20], Layssac *et al.* [24,25] and Billiet *et al.* [23] is schematically depicted in Fig. 1. It consists of a closed-loop refrigerant system and two auxiliary circuits wherein liquid Kryo 20 flows at temperatures controlled by two thermostatic baths. The test fluid is driven in the refrigerant loop by an oil-free gear micropump, and its mass flow rate is measured by a Coriolis mass flow meter. A bypass line connects the inlet and outlet of the micropump, and it is used to set the mass flow rate. A filter dryer is installed in the main loop in order to remove particles dispersed in the test fluid. The refrigerant inside the reservoir is heated by the auxiliary fluid in order to control the saturation pressure at the test section. A needle microvalve is placed upstream the preheater in order to minimize the propagation of pressure fluctuations associated with thermal instability effects during flow boiling in a small diameter channel [52] and ensure a fine adjustment of the saturation pressure and mass flow rate.

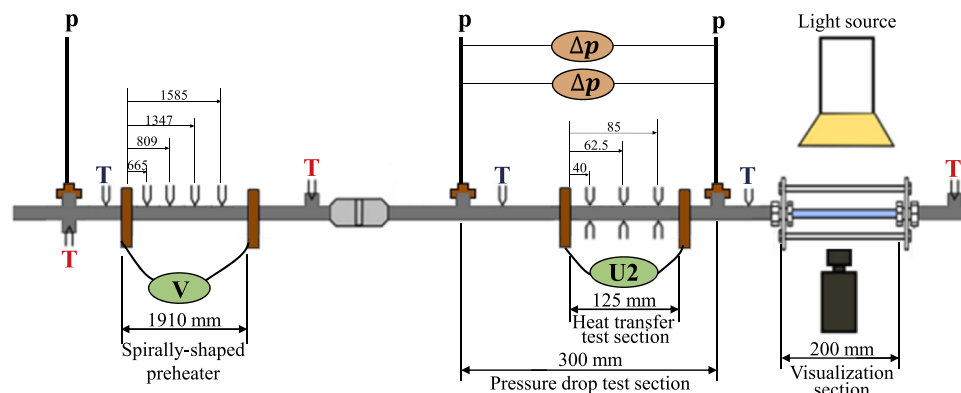


Fig. 2. Schematics of the preheater, test section and visualization section.

The working fluid is heated and evaporated along the preheater and test section. A glass tube is placed downstream of the test section to record the two-phase flow pattern. K-type thermocouples and absolute pressure sensors (Keller® PA23), installed upstream the preheater and downstream the visualization section, are used to measure the refrigerant temperature and pressure, respectively. The working fluid is condensed and subcooled in a plate heat exchanger by exchanging heat with one of the auxiliary circuits. The experimental apparatus was designed to withstand temperatures and pressures up to 120 °C and 30 bar, respectively. The components of the main loop and the pipeline are insulated from the environment through ceramic fiber covered with elastomeric foam.

The preheater, test and visualization sections are schematically presented in Fig. 2. The preheater is a 1910 mm long stainless-steel tube with a spiral shape, having inner and outer diameters of 4 and 6 mm, respectively. The test section is also a stainless-steel tube with an outer diameter of 6 mm, in which two pressure taps are welded 300 mm apart from each other. The inner diameter of the test tube was measured through confocal microscopy, and the average value obtained was 2.07 mm. During pressure drop experiments, the entire test section is kept adiabatic, while for heat transfer coefficient measurements, 125 mm of the tube are heated. The heating effect along the preheater and test section is achieved through Joule effect by directly powering the surface of the tubes through copper electrodes connected to two DC power sources (Sorensen DCS-8-350, SGA 60–250). The visualization section is a 200 mm long Pyrex tube, with inner and outer diameters of 2 and 6 mm, respectively.

The pressure drop is measured by two differential pressure sensors (Endress Hauser® Rosemount 3051) with different measuring ranges (0–50 mbar and 0–2 bar), connected to the pressure taps, as depicted in Fig. 2. Four K-type thermocouples are positioned at the outer surface of the preheater, 665, 809, 1347 and 1585 mm apart from the copper electrode. To assess heat transfer asymmetry during flow boiling, three K-type thermocouples were placed at 90° intervals along the outer perimeter of the test section tube. These thermocouples were positioned at longitudinal distances of 40, 62.5, and 85 mm from the first copper electrode. K-type thermocouples and absolute pressure sensors are used to measure the temperature of the working fluid at the inlet and outlet of each subsection depicted in Fig. 2.

3. Data treatment

This section outlines the data treatment procedure used for evaluating the heat transfer coefficient and the frictional pressure drop. The heat losses estimation procedure is also described in this section, followed by the presentation of the uncertainties of both measured and calculated parameters.

3.1. Heat transfer data reduction

The mass velocity, G , is given as the ratio between the mass flow rate measured by the Coriolis mass flow meter, \dot{m} , and the inner cross-sectional area of the test tube. The local heat transfer coefficient along the test section is evaluated at the positions where the K-type thermocouples are installed, as depicted in Fig. 2. According to the Newton's law, the local HTC is given as follows:

$$h(z) = \frac{\dot{q}_{TS}}{T_{wi}(z) - T_{fluid}(z)} \quad (1)$$

where \dot{q}_{TS} is the internal heat flux, given as:

$$\dot{q}_{TS} = \frac{\dot{Q}_{eff,TS}}{\pi \cdot D_i \cdot L_h} \quad (2)$$

in which D_i is the internal tube diameter, and L_h is its heated length.

The effective test section heating power, $\dot{Q}_{eff,TS}$, is given as the electrical power delivered by the power supply, ($\dot{Q}_{el} = I \cdot U$) minus the heat losses to the environment (\dot{Q}_{loss}):

$$\dot{Q}_{eff,TS} = I \cdot U - \dot{Q}_{loss,TS} = (1 - \eta_{loss,TS}) \cdot I \cdot U \quad (3)$$

where $\eta_{loss,TS}$ is the relative heat losses, whose calculation procedure is described in Section 3.3.

The temperature of the internal surface of the test tube, $T_{wi}(z)$, is calculated according to the solution of the heat diffusion equation assuming uniform heat generation, one-dimensional heat conduction along the radial direction, and adiabatic surface at the outer diameter of the tube, as follows:

$$T_{wi}(z) = T_{wo}(z) + \frac{\dot{q}_{TS}}{16 \cdot k} \cdot (D_o^2 - D_i^2) - \frac{\dot{q}_{TS} \cdot D_o^2}{8 \cdot k} \ln\left(\frac{D_o}{D_i}\right) \quad (4)$$

where k is the stainless-steel thermal conductivity, D_o is the tube outer diameter, and $T_{wo}(z)$ is the temperature measured by the K-type thermocouple attached at the outer surface of the test section at a distance z from the copper electrode. The volumetric heat generation is given by the following relation:

$$\dot{q}_{TS} = \frac{4 \cdot \dot{Q}_{eff,TS}}{\pi \cdot (D_o^2 - D_i^2) \cdot L_h} \quad (5)$$

If the fluid is in a single-phase flow, $T_{fluid}(z)$ is calculated according to an energy balance, as follows:

$$T_{fluid}(z) = T_{in,TS} + \frac{\dot{q}_{TS} \cdot \pi \cdot D_i \cdot z}{\dot{m} \cdot c_p} \quad (6)$$

where c_p is the specific heat capacity of the working fluid.

If two-phase flow is reached, $T_{fluid}(z)$ is equal to the saturation temperature corresponding to the working fluid pressure at position z ($p(z)$). A linear pressure profile is assumed along the two-phase length. Although this approximation is unrealistic, it can be considered valid for the low-pressure drops measured during the HTC experiments (below 10.6 kPa). This is because it does not significantly affect the fluid properties, as previously confirmed by Charnay *et al.* [20].

The working fluid pressure at a distance z from the copper electrode is given as:

$$p(z) = (p_{in,TS} - \Delta p_{1\varnothing}) - \left\{ \left(\frac{\Delta p_{meas} - \Delta p_{1\varnothing}}{L_{\Delta p} - L_{1\varnothing}} \right) \cdot [z + L_{adiabatic} - L_{1\varnothing}] \right\} \quad (7)$$

where $p_{in,TS}$ is the pressure measured by the absolute pressure sensor upstream the test section, Δp_{meas} is the measured pressure drop, $L_{\Delta p}$ is the distance between the pressure taps in which the differential pressure sensors are connected, and $L_{adiabatic}$ is the adiabatic length upstream the first copper electrode. If the working fluid is subcooled at the preheater outlet, the single-phase pressure drop, $\Delta p_{1\varnothing}$, along the test section subcooled length ($L_{1\varnothing}$) is calculated according to Blasius correlation, otherwise, $\Delta p_{1\varnothing} = 0$ and $L_{1\varnothing} = 0$.

The local vapor quality is estimated according to the following relation:

$$x(z) = \frac{i(z) - i_l(p(z))}{i_v(p(z)) - i_l(p(z))} \quad (8)$$

where $i_l(p(z))$ and $i_v(p(z))$ are the liquid and vapor specific enthalpies, respectively. The local working fluid specific enthalpy, $i(z)$, is calculated as follows:

$$i(z) = i_{in,TS} + \frac{\dot{q}_{TS} \cdot \pi \cdot D_i \cdot z}{\dot{m}} \quad (9)$$

in which the inlet specific enthalpy is given by a heat balance along the preheater, as follows:

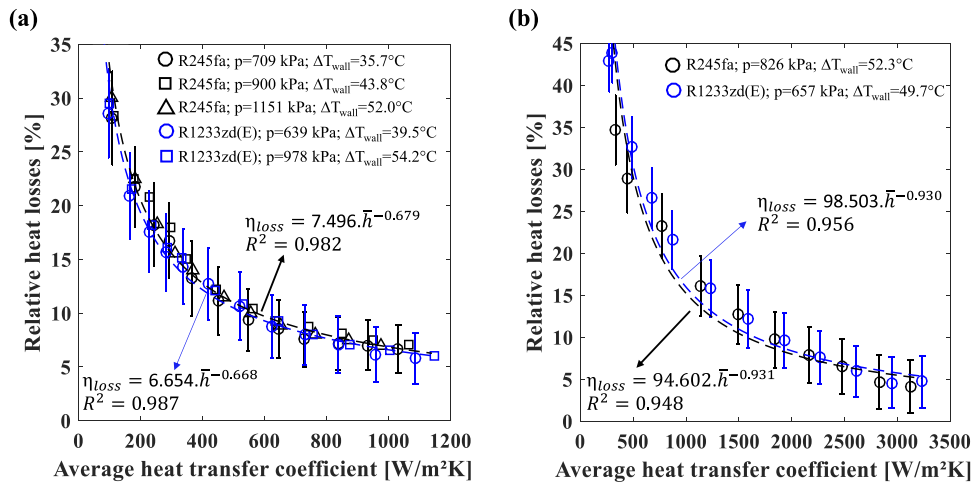


Fig. 3. Effect of the average heat transfer coefficient on the relative heat losses along the (a) preheater and (b) test section ($\Delta T_{wall} = \bar{T}_{wo} - T_{amb}$).

$$i_{in,TS} = i_{in,PH} + \frac{\dot{Q}_{eff,PH}}{\dot{m}} \quad (10)$$

where $\dot{Q}_{eff,PH}$ is the preheater effective heating power and $i_{in,PH}$ is the liquid saturated specific enthalpy corresponding to the temperature measured at the preheater inlet.

As previously mentioned, 3 thermocouples, placed 90° apart are attached at each HTC longitudinal measuring position. Therefore, the average local heat transfer coefficient is given as:

$$\bar{h}(z) = \frac{(h(z)_{top} + 2h(z)_{middle} + h(z)_{bottom})}{4} \quad (11)$$

where the subscripts *top*, *middle* and *bottom* correspond to the top, middle and bottom circumferential positions, respectively.

3.2. Adiabatic pressure drop data reduction

The frictional pressure gradient is given by the following relation:

$$\left(\frac{dp}{dz}\right)_f = \frac{\Delta p_f}{L_{\Delta p}} \quad (12)$$

where $L_{\Delta p}$ is the distance between the pressure taps at which the differential pressure sensors are connected.

The frictional pressure drop (Δp_f) is given as the measured pressure drop (Δp_{meas}) minus the accelerational parcel (Δp_{accel}). During single-phase flow, Δp_{accel} is negligible, while for two-phase flow it is given as:

$$\Delta p_{accel} = G^2 \cdot \left\{ \left[\frac{x^2}{\alpha \cdot \rho_v} + \frac{(1-x)^2}{(1-\alpha) \cdot \rho_l} \right]_{out} - \left[\frac{x^2}{\alpha \cdot \rho_v} + \frac{(1-x)^2}{(1-\alpha) \cdot \rho_l} \right]_{in} \right\} \quad (13)$$

where α is the void fraction, ρ_l and ρ_v are the liquid and vapor phase densities, and the subscripts *in* and *out* represent the inlet and outlet of the pressure drop measuring sections, respectively.

Pressure drop experiments were conducted under adiabatic flow conditions. Therefore, the accelerational contribution is solely linked to the flashing effect, resulting from the increase in vapor quality due to the expansion of the vapor phase caused by pressure reduction along the test section. In the present investigation, the maximum measured adiabatic pressure drop was 17.9 kPa, therefore, the increase of vapor quality along the test tube is marginal. According to the correlation developed by Revellin et al. [53] for predicting the vapor quality increment due to the flashing effect, the maximum increment during the experiments was 0.006. Therefore, Δp_{accel} contribution was always lower than 2% of the measured pressure drop, which is close to the average uncertainty of

Δp_{meas} , 2.1%. Therefore, the accelerational contribution was considered negligible during the adiabatic pressure drop investigation.

The vapor quality at the pressure drop measuring section inlet is given by the following relation:

$$x_{in,TS} = \frac{i_{in,TS} - i_l(p_{in,TS})}{i_v(p_{in,TS}) - i_l(p_{in,TS})} \quad (14)$$

where $i_l(p_{in,TS})$ and $i_v(p_{in,TS})$ are the liquid and vapor phase specific enthalpies of the working fluid evaluated at the test section inlet pressure ($p_{in,TS}$). It is important to remark that, heat losses in the test section during adiabatic pressure drop experiments were neglected. This assumption was previously verified considering a thermal resistance network and heat balance calculations. The vapor quality uncertainties were 1.2–6.4 times higher than the decrease of x associated to the estimated heat losses. This fact supports the above-mentioned assumption.

Fluid properties were obtained from REFPROP v. 10 [54] and some of their values are presented in Table 2.

3.3. Heat losses evaluation

The preheater and test section heat losses were estimated during single-phase flow experiments. The electrical power delivered by the power supplies were compared with the enthalpy variation of the fluid, and the relative losses were estimated according to the following relation:

$$\eta_{loss} = \frac{I \cdot U - \dot{m} \cdot (i_{out} - i_{in})}{I \cdot U} \quad (15)$$

where i_{in} and i_{out} are the inlet and outlet specific enthalpies of the fluid at the test section or preheater, respectively.

The relative heat losses were correlated as functions of the average heat transfer coefficient along the tube length according to power laws ($\eta_{loss} = a \cdot \bar{h}^b$) for both preheating and test sections. In this case, \bar{h} is given by the arithmetic mean between all the HTCs measured along the tube length (4 measurements for the preheater and 3 for the heat transfer test section). Fig. 3 presents the experimental results obtained and the corresponding curve fits determined through the least squares method for both preheating and test sections. The analytical expressions indicate that the relative heat losses are inversely proportional to the average heat transfer coefficient ($b < 0$), which is associated with the overall thermal resistance reduction with increasing \bar{h} .

The equations adjusted for η_{loss} , are also used during two-phase flow experiments, but an iterative procedure is necessary, since \bar{h} is calcu-

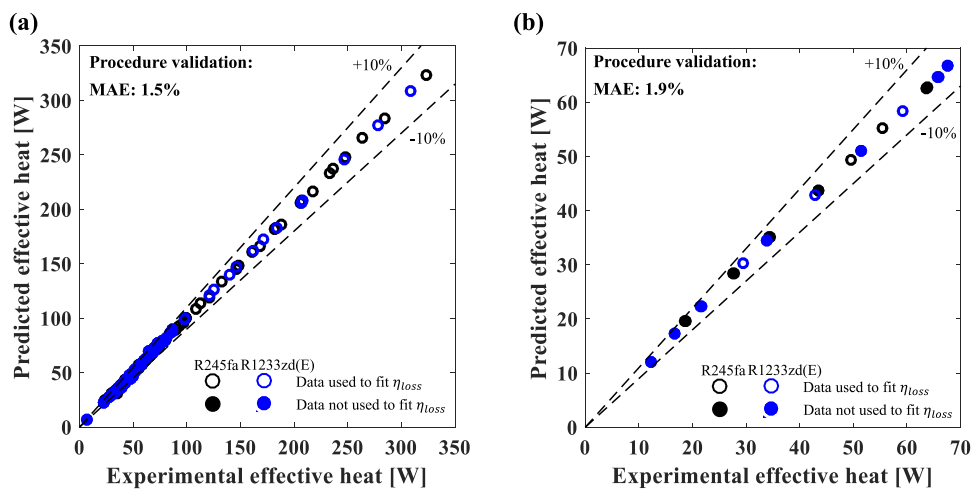


Fig. 4. Validation of the heat losses calculation procedure at (a) preheater and (b) test section.

Table 3
Uncertainties of the sensors and instruments of the experimental bench.

| Instrument | Measured parameter | Range | Uncertainty |
|---------------------|--------------------------|------------------|------------------------|
| Keller PA23 | Absolute pressure | 0–3000 kPa | 6 kPa |
| Rosemount 3051S | Differential pressure | 0–5 kPa | 0.005 kPa |
| Rosemount 3051S | Differential pressure | 0–200 kPa | 0.2 kPa |
| K-type thermocouple | Temperature | 25–115 °C* | 0.15 °C |
| Micromotion CMF | Mass flow rate | 0–108 kg/h | 0.1% of measured value |
| Sorensen DCS | Voltage drop and current | 0–8 V/ 8–350 A | 12 mV/1.4A |
| Sorensen SGA | Voltage drop and current | 0–60 V/ 60–250 A | 60 mV/1A |

* Calibration range.

lated based on the effective heat flux (Eq. (1)). As an initial guess, the heat losses during two-phase flow at a given mass velocity are assumed equal to η_{loss} for single-phase flow at the same G . Then, the effective heat flux is calculated, as well as \bar{h} , and a new value for η_{loss} is assigned. This procedure is repeated until two subsequent iterations present a difference lower than 0.005 for η_{loss} . In order to validate the iterative procedure, the effective heating power calculated based on energy balance during single-phase flow experiments was compared against the corresponding predicted value through the iterative procedure. The results of this comparison are presented in Fig. 4, and the average error between real and predicted effective heating power were 1.5 and 1.9% for the preheater and the test sections, respectively.

3.4. Experimental uncertainties

The experimental setup described in Section 2 is monitored and controlled using a personal computer with a LabVIEW (National Instruments®) interface. Signals from the thermocouples, pressure transducers, mass flow meter and supplied electrical voltage to the preheater and the test section are acquired by a Keithley data acquisition system model 2701, with two slot cards (7702 and 7706 models). The K-type thermocouples are connected to a cold junction compensation system, which contains a platinum Pt100 used as temperature reference. Thermocouples calibration was performed prior to experiments for a temperature range of 25–115 °C using a model 9142 Fluke® calibration device. Temperature uncertainties were evaluated according to the procedure proposed by Abernethy and Thompson Jr. [55], which considers a confidence level of 95%. For the remaining sensors and measuring devices, the uncertainties were assumed equal to the specifications provided by the manufacturers. Table 3 presents the

Table 4
Uncertainties of the main experimental parameters.

| Parameter | Uncertainty | Parameter | Uncertainty |
|-----------|-------------|-------------|-------------|
| D_t | 0.048 mm | q'_T | 6.5% |
| L_h | 1 mm | T_{wo} | 0.15 °C |
| \dot{m} | 0.1% | h_z | 10.1% |
| p | 6 kPa | $(dp/dz)_f$ | 2.1% |
| G | 4.6% | x_z | 0.035 |

uncertainties of the sensors and instruments installed in the experimental setup.

The uncertainties of the calculated parameters were estimated according to the sequential perturbation method [56]. Table 4 summarizes the average uncertainties of the main experimental parameters.

4. Validation

The validation of the experimental bench and the data treatment procedure was performed based on single-phase experiments. Firstly, pressure drop experiments were performed without applying electrical power to the test section. Fig. 5a presents the comparison between the fanning friction factor calculated from the experimental data and the predictions based on Blasius correlation. A reasonable agreement is verified between experimental and predicted values, with all data predicted within an error margin lower than $\pm 14\%$, and a MAE of only 10.4%.

Single-phase heat transfer experiments were also performed at the test section during the validation stage. Fig. 5b presents the comparison of the R245fa experimental Nusselt number against prediction methods from literature [57–60]. Single-phase heat transfer results were obtained for mass velocities varying from 187 to 1867 kg/m²s, heat fluxes of 9.6–86.8 kW/m², and inlet temperatures between 39 and 41 °C. The method proposed by Churchill and Ozoe [60] for developing flow predicted laminar data ($Re < 2300$) with an error close to 2%, as verified in Fig. 5b. Considering turbulent data ($Re \geq 2300$), high deviations are verified for $Re=2300$ –5000, which may be associated with the transition zone between laminar and fully turbulent. As the Reynolds number increases, a reasonably agreement is verified between the experimental data and the prediction methods, especially for the correlations of Colburn [58], Gnielinski [57] and Dittus-Boelter.

5. Flow patterns

During the evaluation of pressure drop and heat transfer coefficient,

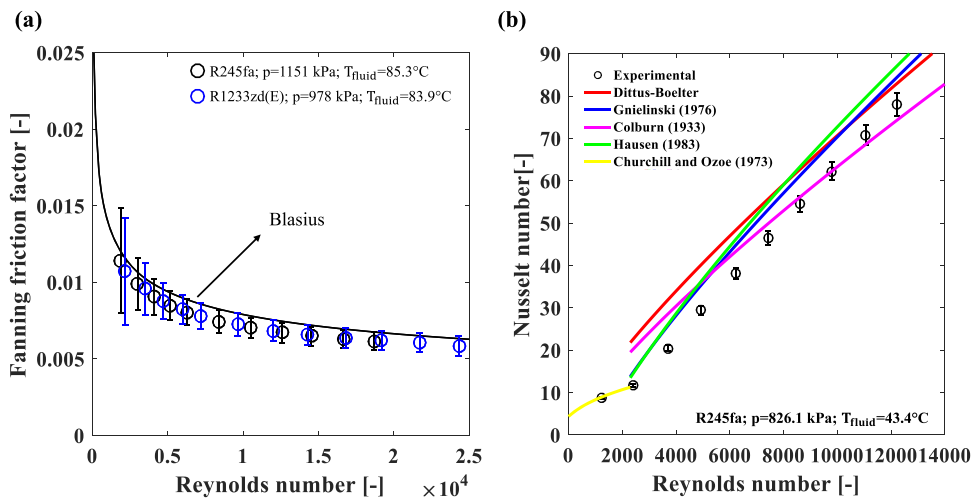


Fig. 5. (a) Comparison between experimental single-phase friction factor and Blasius correlations; (b) Comparison between single-phase experimental Nusselt number against prediction methods.

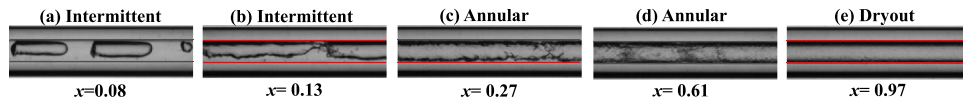


Fig. 6. Flow pattern evolution with increasing vapor quality ($R1233zd(E)$, $T_{sat}=75\text{ }^{\circ}\text{C}$, $G = 373\text{ kg/m}^2\text{s}$, $q''=36.6\text{ kW/m}^2$).

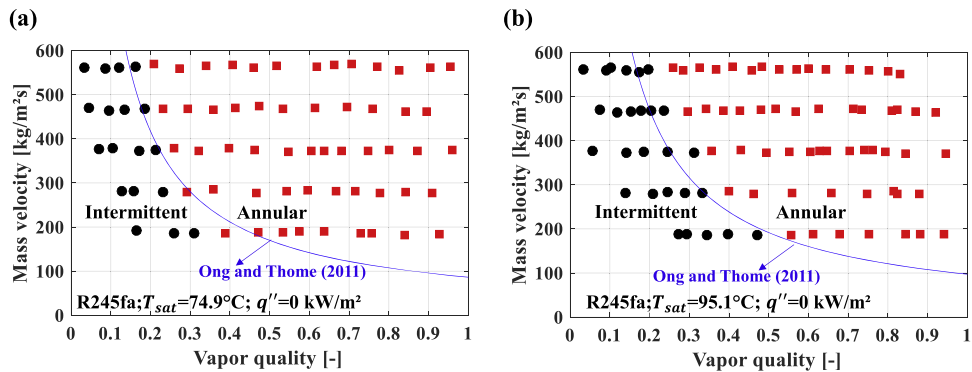


Fig. 7. Mass velocity effect on the intermittent-annular transition at (a) $T_{sat}=74.9\text{ }^{\circ}\text{C}$ and (b) $T_{sat}=95.1\text{ }^{\circ}\text{C}$.

the flow patterns along the Pyrex tube were recorded using a high-speed camera (Photron® FASTCAM SA3 120 K M2). The image acquiring rate was set to 2000 frames/s, the shutting speed was 1/30,000 s and the acquisition time 2.2515s.

Intermittent and annular flow patterns were identified based on the images recorded. The onset of liquid film dryout was quantified by a sudden drop in the heat transfer coefficient. Fig. 6 presents the evolution of the flow patterns visualized for R1233zd(E) at $G=373\text{ kg/m}^2\text{s}$, $T_{sat}=75\text{ }^{\circ}\text{C}$ and $q''=36.6\text{ kW/m}^2$ with increasing vapor quality. It is important to remark that, at very low vapor qualities, plug flow pattern is verified (Fig. 6a), while with a slight increment of x , slug flow was typically identified (Fig. 6b), however, for simplicity, both flow patterns were classified as intermittent. Despite the small diameter of the test tube, stratification effects are still verified, indicated by the thicker liquid film at the bottom of the tube, evident in Fig. 6c.

Fig. 7 presents the mass velocity effect on the intermittent-annular transition at two different saturation temperatures. As well as reported at low T_{sat} studies [61–64]. The increase in mass velocity anticipates this flow pattern transition. Comparing Figs. 7a and 7b, it is verified that increasing T_{sat} postpones the intermittent-annular transition. According to Yang *et al.* [64], the increase of saturation temperature results in

lower surface tension, therefore, it is difficult for liquid holdup to the tube perimeter to form the annular flow. Fig. 7 also presents the lines corresponding to the transition criteria proposed by Ong and Thome [63]. At $T_{sat}=75\text{ }^{\circ}\text{C}$ the prediction method of Ong and Thome [63] seems to be more accurate in predicting the intermittent-annular transition for high mass velocities, however, at $T_{sat}=95\text{ }^{\circ}\text{C}$, a better agreement is verified for mass velocities of 187 and 280 $\text{kg/m}^2\text{s}$.

6. Adiabatic pressure drop

In the present study, 450 adiabatic frictional pressure gradient datapoints were obtained for saturation temperatures of 75–95 $^{\circ}\text{C}$ and mass velocities from 180 to 570 $\text{kg/m}^2\text{s}$. These data cover intermittent and annular flow patterns. Since the last thermocouple attached to the preheater surface was placed relatively far from its outlet (325 mm) it was impossible to identify the sharp increase of the surface temperature. Therefore, the post-dryout conditions were not differentiated from annular flow during pressure drop experiments. This section describes the effects of G and T_{sat} on the frictional pressure gradient, followed by a comparison of the dataset obtained in the present study against 20 two-phase frictional pressure drop prediction methods.

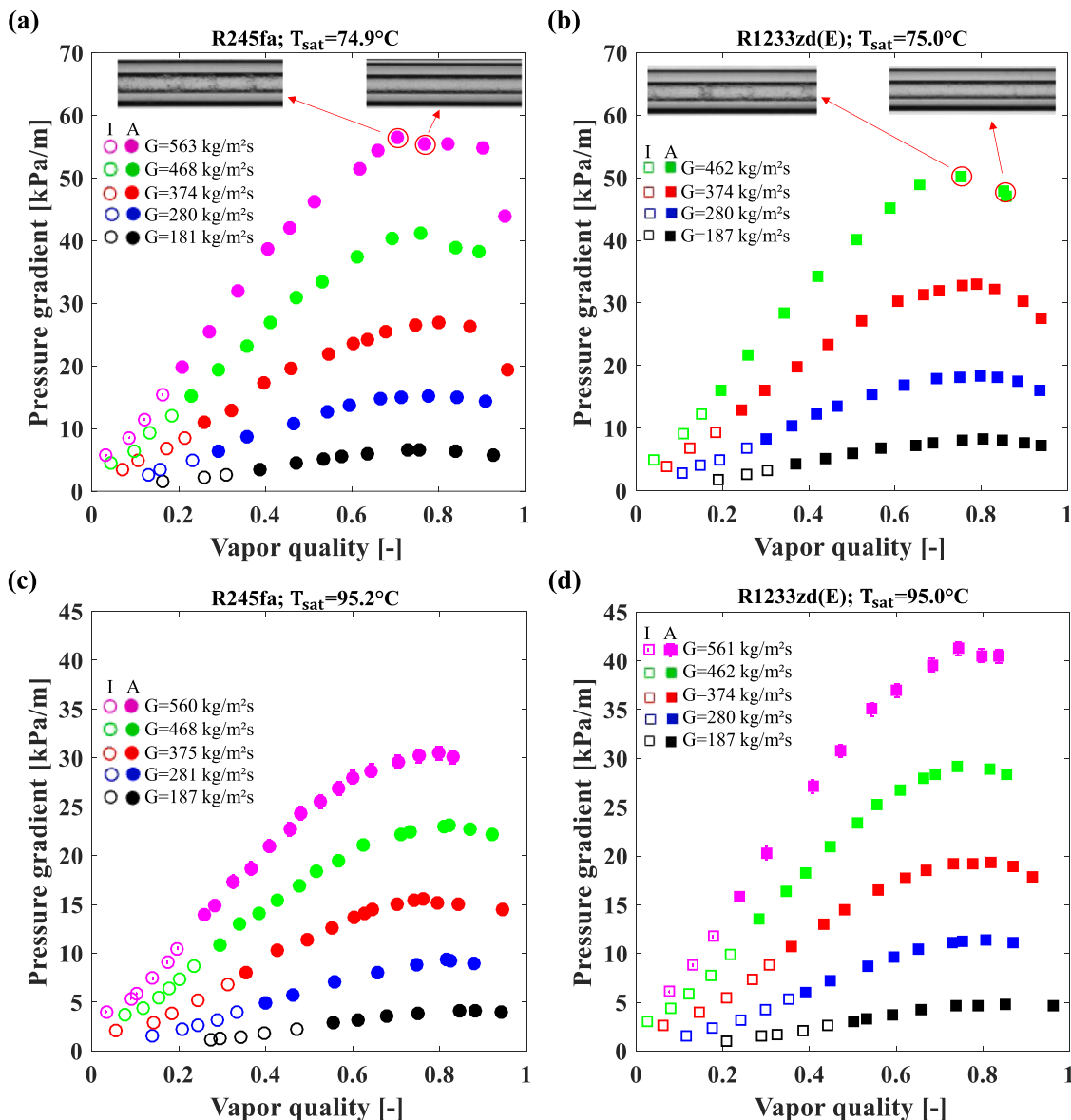


Fig. 8. Mass velocity effect on the frictional pressure gradient for (a)R245fa, $T_{sat}=74.9^{\circ}\text{C}$, (b) R1233zd(E), $T_{sat}=75.0^{\circ}\text{C}$, (a)R245fa, $T_{sat}=95.2^{\circ}\text{C}$, (b) R1233zd(E), $T_{sat}=95.0^{\circ}\text{C}$ (I: Intermittent flow, A: Annular flow).

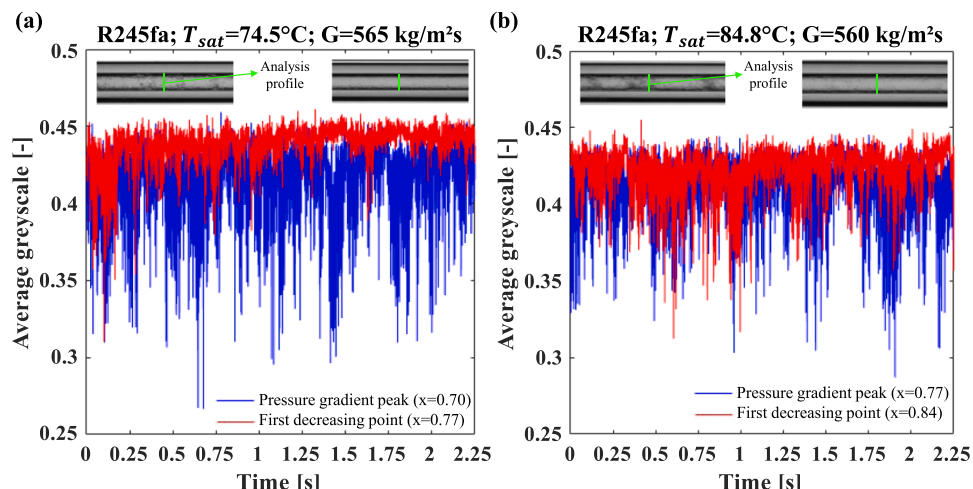


Fig. 9. Qualitative analysis of interfacial wave before and after pressure gradient trough greyscale variation along time.

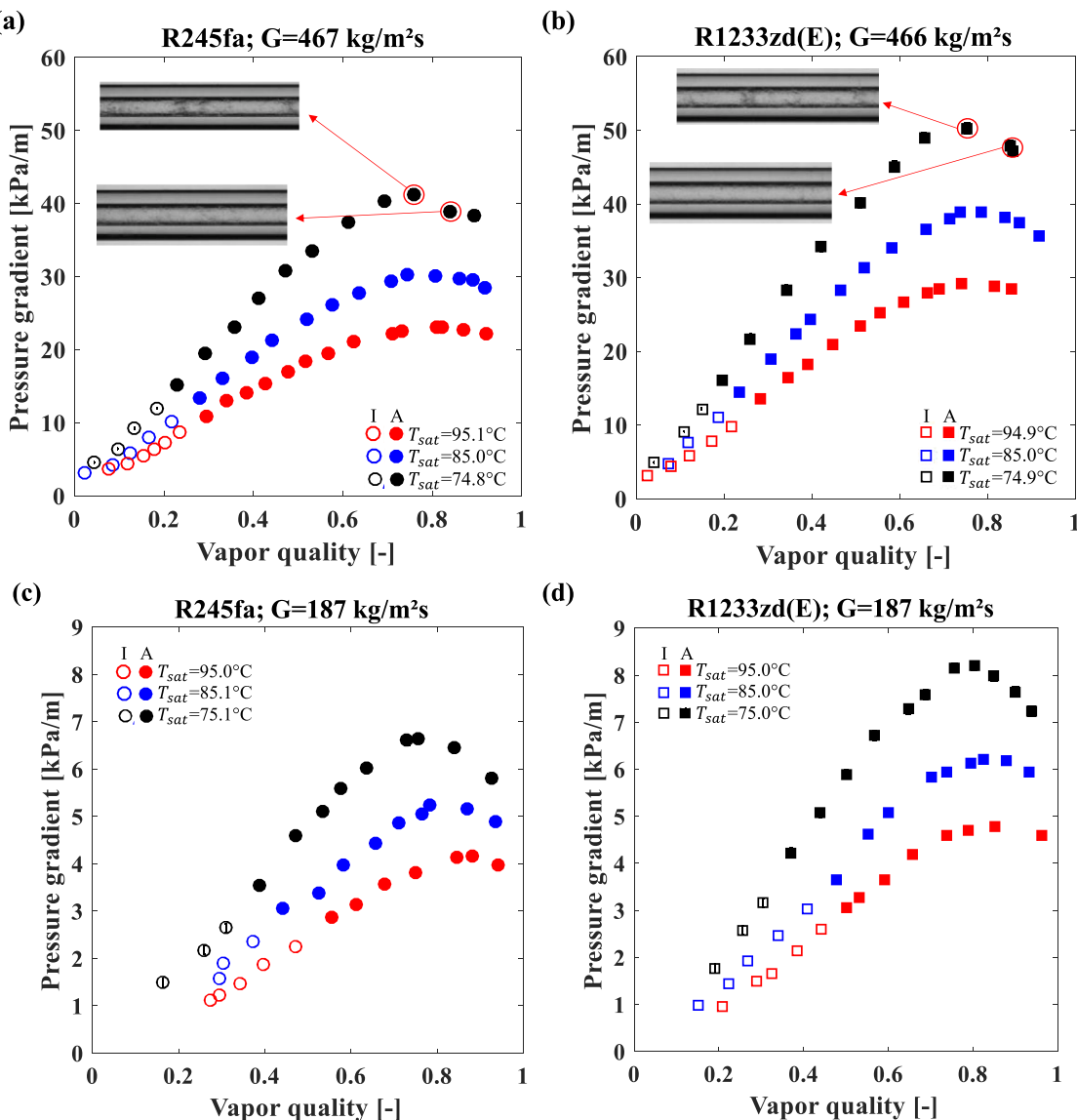


Fig. 10. Saturation temperature effect on the frictional pressure gradient for (a)R245fa, $G = 467 \text{ kg/m}^2\text{s}$, (b) R1233zd(E), $G = 466 \text{ kg/m}^2\text{s}$, (a)R245fa, $G = 187 \text{ kg/m}^2\text{s}$, (b) R1233zd(E), $G = 467 \text{ kg/m}^2\text{s}$ (I: Intermittent flow, A: Annular flow).

6.1. Frictional pressure gradient experimental results

Fig. 8 presents the effect of G on the frictional pressure gradient for both R1233zd(E) and R245fa. As verified in Fig. 8, all the experimental results present the same behavior with varying vapor quality, which is similar to those typically verified in the literature for lower saturation temperatures. The two-phase frictional pressure gradient increases with the increment of x , due to the two-phase viscosity reduction and increment of two-phase specific volume, resulting in the increase of flow velocity and shear. This behavior is maintained until the pressure gradient reaches its maximum, from which it starts to decrease with subsequent increments of vapor quality.

As pointed out by Marchetto et al. [13], three different explanations for the $(dp/dz)_f$ reduction at high x are reported in the literature: (i) liquid film dryout; (ii) transition to mist flow pattern; (iii) damping of the disturbance waves at the liquid film interface. The flow images recorded for the first datapoints after the $(dp/dz)_f$ peak (Figs. 8a and 8b) indicate that a thin smooth liquid film is still verified along the tube perimeter. A qualitative investigation of the interfacial wave amplitude was performed through image analysis, as depicted in Fig. 9. A profile line was placed from the bottom to the top of the tube inner diameter

and the average greyscale value of the pixels positioned in this line was calculated for each frame. In the present work, a normalized greyscale scale was adopted, with the values ranging from 0 to 1. The variations of the average greyscale value during the recording time for different experimental conditions are presented in Fig. 9a and 9b. It can be verified that the greyscale oscillations were considerably reduced for the datapoints after the pressure gradient peak, indicating that the decrease of $(dp/dz)_f$ should be associated with disturbance waves damping. Experimental results obtained by Moreira et al. [65] displayed similar behavior for R245fa flowing in a rectangular channel at $T_{sat}=23^\circ\text{C}$.

The experimental results indicate that the pressure gradient increases with rising G . Such an effect is associated to the two-phase flow velocity increase and, consequently, the increment of shear effects. The increase of mass velocity also seems to anticipate the pressure gradient peak to lower vapor qualities, a behavior that was also reported by Charnay et al. [19], Lillo et al. [26] and Arcasi et al. [31]. This effect might be associated with the higher entrainment rate at high mass velocities, anticipating the damping of disturbance waves at the interface [66].

The effect of the saturation temperature on the frictional pressure gradient is presented in Fig. 10. The reduction of $(dp/dz)_f$ with rising T_{sat}

Table 5

Mean average errors resulting of the comparison between the pressure drop data and prediction methods.

| Authors | MAE (%) | | | Experimental conditions covered by the database used to the development of the method |
|--|----------|--------|-------------|--|
| | All data | R245fa | R1233zd (E) | |
| <u>Homogeneous methods</u> | | | | |
| McAdams et al. [67] | 34.1 | 33.5 | 34.6 | Benzene-oil |
| Cicchitti et al. [68] | 19.2 | 17.9 | 20.6 | – |
| Dukler et al. [69] | 36.6 | 35.6 | 37.7 | D_H : 12.3–127 mm; 2620 data points |
| Beattie and Whalley [70] | 29.7 | 28.2 | 31.2 | Adiabatic; C/S/H/V; 13,510 data points |
| Lin et al. [71] | 31.1 | 30.4 | 31.8 | Adiabatic; C/S/H; R12; D_H : 0.66–1.17 mm; p_r : 0.15–0.32; G: 1440–5090 kg/m ² s; 238 data points |
| Garcia et al. [72] | 35.3 | 32.8 | 38.0 | Air-oil, air-kerosene, air-water, gas-liquid hydrocarbon; C/S/H; D_H : 23.2–140.2 mm; 2435 data points |
| Awad and Muzychka [73] v.1 | 20.5 | 19.3 | 21.8 | Adiabatic/Evaporation; C,R,S,M/H; R12, R22, R134a, R410A, R290, argon, ammonia; D_H : 0.15–14 mm; p_r : 0.07–0.49 |
| Awad and Muzychka [73] v.2 | 28.8 | 28.0 | 29.6 | |
| Ducoulombier et al. [74] | 26.1 | 25.8 | 26.4 | Adiabatic; C/S/H; CO ₂ ; D_H : 0.53 mm; p_r : 0.36–0.54; G: 200–1400 kg/m ² s; 608 data points |
| <u>Two-phase multiplier-based methods</u> | | | | |
| Friedel [41] | 23.6 | 22.4 | 24.9 | C,R/S/H,V; Air/water, air/oil, R12; D_H >4 mm; 25,000 data points |
| Mishima and Hibiki [75] | 31.2 | 33.3 | 28.9 | C,R/S/V; Air/water; DH: 1–4 mm; p: 101.3 kPa |
| Zhang and Webb [14] | 15.4 | 13.3 | 17.6 | Adiabatic; C/S,M/H; R22, R134a, R4404A; D_H : 2.13–3.25 mm; p_r : 0.21–0.51; G: 400–1000 kg/m ² s |
| Ducoulombier et al. [74] | 156.3 | 121.2 | 193.7 | C/S/H; CO ₂ ; D_H : 0.529 mm; p_r : 0.36–0.54; G: 200–1400 kg/m ² s; 608 data points |
| Kim and Mudawar [76] | 16.8 | 15.9 | 17.6 | Adiabatic/Evaporation; C,R,S,M/H,V; R12, R134a, R22, R245fa, R410A, FC-72, ammonia, CO ₂ , water; D_H : 0.349–5.35 mm; p_r : 0.005–0.78; G: 33–2738 kg/m ² s; 2378 data points |
| Nie et al. [77] | 12.2 | 11.3 | 13.2 | Adiabatic/Evaporation/Condensation; C/S/H; ethanol, methane, nitrogen, R123, R1234yf, R1234ze(E), R1270, R134a, R14, R152a, R22, R245fa, R290, R32, R402A, R404A, R407C, R410A, R452B, R455A, R502, R600a, R601, ammonia, CO ₂ ; D_H : 0.24–14.45 mm; p_r : 0.01–0.95; G: 50–2000 kg/m ² s; 8663 data points |
| <u>Empirical methods</u> | | | | |
| Müller-Steinhagen and Heck [43] | 14.8 | 13.8 | 15.9 | Adiabatic; C/S/H,V; Water, hydrocarbons, Air/water, water/argon, air/oil, R11, R12, R22, argon, nitrogen, neon, air/water/carboxyl methyl cellulose; D_H : 4–392 mm; 9313 data points |
| Xu and Fang [78] | 22.0 | 19.7 | 24.5 | Evaporation; C,R,F/S,M/H,V; R11, R12, R134a, R22, R32/R125, R123, CO ₂ , R407C, R410A, R404A, R507, R507A, R417A, ammonia, D_H : 0.81–19.1 mm; p_r : 0.36–0.54; G: 25.4–1150 kg/m ² s; 2622 data points |
| Sempértegui-Tapia and Ribatski [79] | 18.9 | 17.2 | 20.6 | Adiabatic; C,R,T/S/H; R134a, R1234yf, R1234ze(E), R600a; D_H : 0.634–1.1 mm; p_r : 0.11–0.31; G: 100–1600 kg/m ² s; 1468 data points |
| Tibiriçá et al. [80] | 20.7 | 19.5 | 22.2 | Adiabatic/Evaporation; C,R,T,S,M/H; R12, R134a, R22, R404A, R410A, R236fa, air/water, CO ₂ , R290, R245fa, R1234ze(E), R1234yf, R600a, ammonia; p_r : 0.05–0.54; D_H : 0.509–3.25 mm; G: 100–7700 kg/m ² s; 1076 data points |

C: Circular; R: Rectangular; F: Flattened; T: Triangular; S: Single-channel; M: Multi-channels; H: Horizontal; V: Vertical.

is associated with the increase of the vapor density, which reduces the two-phase velocity. Furthermore, as the system approaches the critical point, the approximation of vapor and liquid densities (ρ_v and ρ_l) also reduces interfacial shear, as the difference between the velocities of the phases decreases

Comparing the experimental results for both refrigerants, it is verified that at the same T_{sat} and G, the R1233zd(E) presented higher pressure gradients than those for the R245fa, which is associated with the lower reduced pressure of the first refrigerant, as verified in Table 2. The latter shows also that the vapor phase density of the R1233zd(E) is 20% lower than that for the R245fa at $T_{sat}=75$ °C, and 22% at 95 °C. Furthermore, the densities ratio (ρ_l/ρ_v) is 19% and 22% higher for the R1233zd(E) at $T_{sat}=75$ °C and 95 °C, respectively.

6.2. Frictional pressure gradient prediction methods evaluation

The experimental results obtained in the present study were compared against twenty frictional pressure gradient prediction methods, classified as: based on the homogeneous model, based on two-phase multipliers, and empirical correlations. Table 5 presents the experimental conditions for which these methods were developed, as well as the corresponding mean average errors resulting from the comparisons.

In general, the difference of the mean average errors between the two working fluids remained between 1 and 5%, with only the method of Mishima and Hibiki [75] presenting a clear higher accuracy for R245fa. However, the two-phase multiplier-based method of Ducoulombier et al. [74] showed a MAE 72.5% higher for R1233zd(E), which is associated to the strong inaccuracy of this method when applied at p_r lower than those for which it was proposed ($p_r = 0.36 – 0.54$). Since the reduced

pressures evaluated for the R1233zd(E) were lower, it is reasonable that the MAE for this fluid becomes higher.

Fig. 11 displays the comparisons between experimental data and the corresponding predictions for the six methods that presented MAEs lower than 20%. The method proposed by Nie et al. [77] predicted the largest parcel of data within a ±30% error band (97.6%), and also presented the lowest MAE, 12.2%. As verified in Fig. 11a the accuracy of this method was progressively improved as the saturation temperature increases. The extensive database used by Nie et al. [77] to develop their correlation includes a relevant number of datapoints at intermediate-to-high reduced pressures, not only for CO₂, but also for organic refrigerants, which may justify the accuracy of this method. No relevant effect of the saturation temperature on the accuracy of the methods of Muller-Steinhagen and Heck [43], Sempértegui-Tapia and Ribatski [79], Cicchitti et al. [68] and Zhang and Webb [14] (Figs. 11b, 11c, 11e, 11f) was verified, while the method proposed by Kim and Mudawar [76] presented less accuracy as T_{sat} increases (Fig. 11d). It is also important to remark that, 7 of the 9 homogeneous-based prediction methods presented reduction of the MAE as T_{sat} increases. Such a behavior seems associated to the reduction of the slip ratio as the experimental conditions approach to the critical point.

Despite the reduced deviations provided by some of the evaluated methods, none of them accurately predicted the vapor quality corresponding to the maximum pressure gradient (x_{max}). Fig. 12 presents the comparison between experimental data and the predictions according to the six best methods, in which the overestimation of x_{max} can be verified for all of them. It can also be noticed in Fig. 12 that the homogeneous model combined with the correlation for the two-phase viscosity as proposed by Cicchitti et al. [68] is highly accurate at low vapor qualities, in which intermittent flow patterns are typically verified, while at

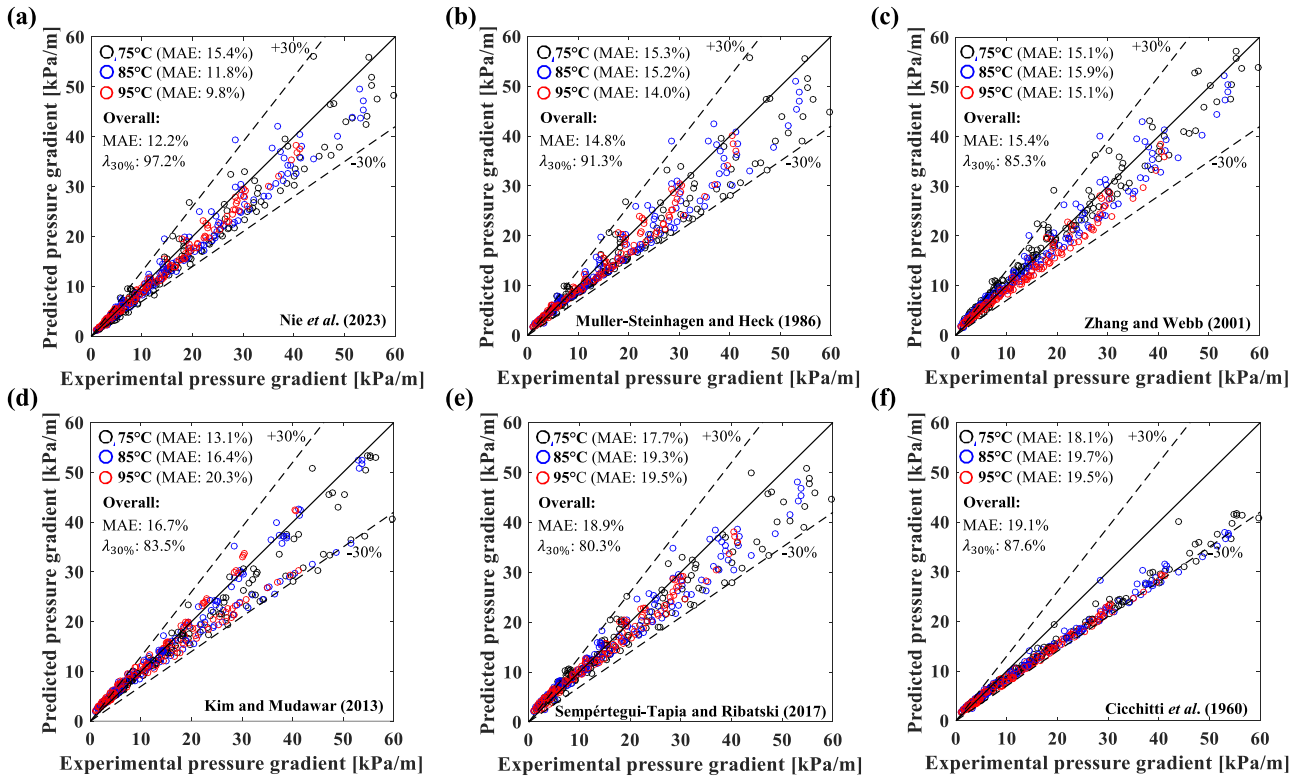


Fig. 11. Comparison between experimental pressure gradient and predictions according to (a) Nie et al. [77], (b) Muller-Steinhagen and Heck [43], (c) Zhang and Webb [14], (d) Kim and Mudawar [76], (e) Sempértegui-Tapia and Ribatski [79] and (f) Cicchitti et al. [68].

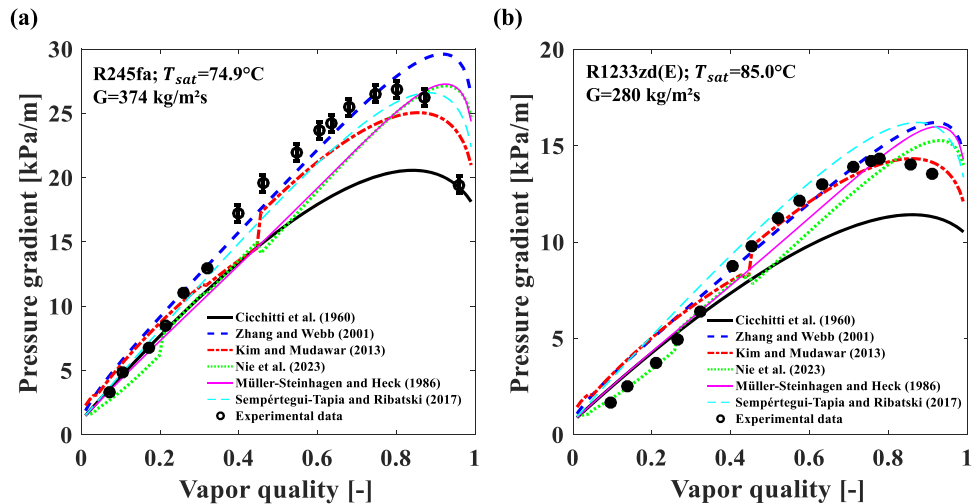


Fig. 12. Comparison between experimental data and prediction methods. (a) R245fa, $T_{sat}=74.9^{\circ}\text{C}$, $G=374 \text{ kg/m}^2\text{s}$; (b) R1233zd(E), $T_{sat}=85.0^{\circ}\text{C}$, $G=280 \text{ kg/m}^2\text{s}$.

intermediate-to-high x , this method underestimated the experimental data. In fact, a similar behavior was verified for 7 of the 9 methods based on the homogeneous model, for which the MAEs for intermittent flow data were 3.6%–23.9% lower than those for annular flows. The separation of liquid and vapor phases during annular flow, increasing shear effects and diverging from the hypotheses of the homogenous model, seems associated to such a behavior.

7. Heat transfer coefficient

In the present study, experimental results for the heat transfer coefficient were obtained for R245fa and R1233zd(E) at saturation temperatures between 75 and 95 °C, mass velocities from 176 to 378 kg/

m^2s , and heat fluxes of 18.1–54.5 kW/m². This section analyses the effects of q' , G and T_{sat} on the heat transfer coefficient and presents comparisons of the dataset obtained in the present study against 16 flow boiling HTC prediction methods.

7.1. Analysis of the heat transfer coefficient results

Fig. 13 presents the effect of the heat flux on the heat transfer coefficient for R1233zd(E) at two different saturation temperatures. At both T_{sat} , the HTC increases with increasing the heat flux. Such a behavior was already expected and is associated with the easier activation of nucleation sites on the heated surface, which intensifies the bubbles nucleation activity. In general, the HTC presented a slight

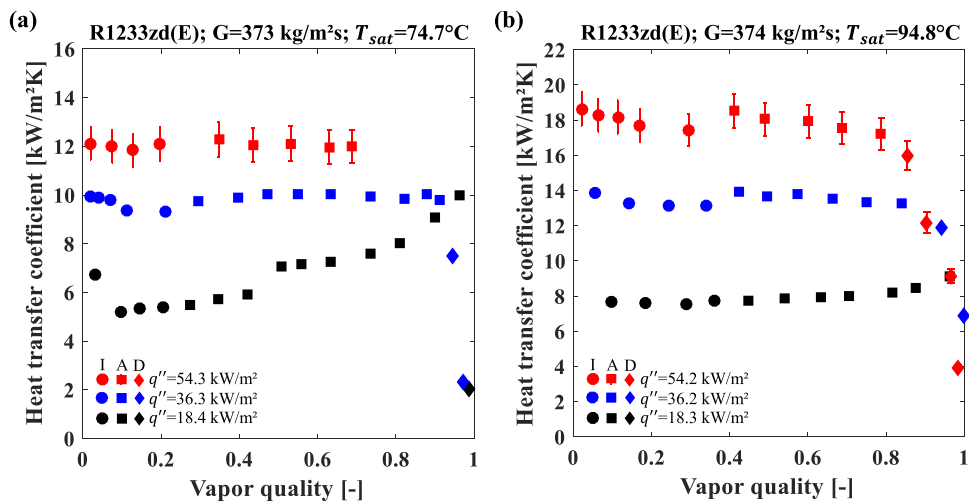


Fig. 13. Heat flux effect on the heat transfer coefficient for R1233zd(E) at (a) $G = 373 \text{ kg/m}^2\text{s}$, $T_{sat}=74.7^\circ\text{C}$ and (b) $G = 374 \text{ kg/m}^2\text{s}$, $T_{sat}=94.8^\circ\text{C}$ (I: Intermittent flow, A: Annular flow, D: Dryout).

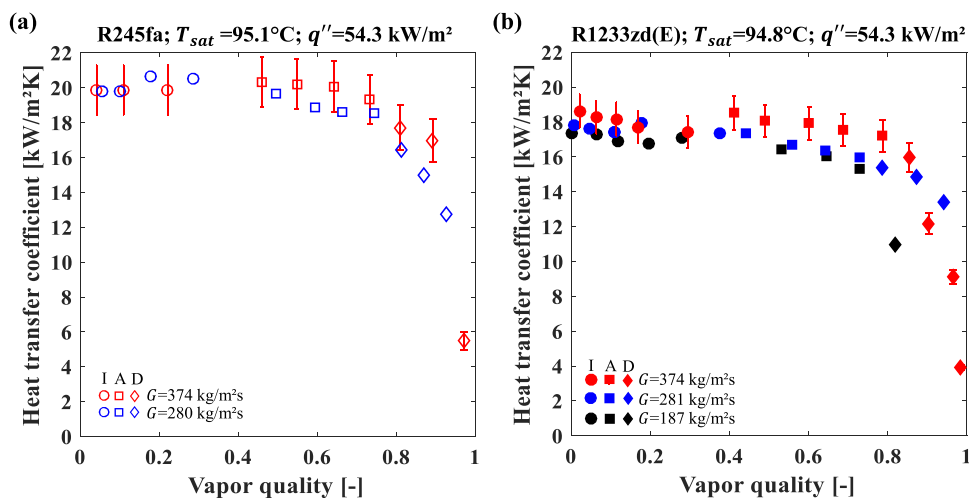


Fig. 14. Mass velocity effect on the heat transfer coefficient for (a) R245fa, $T_{sat}=95.1^\circ\text{C}$, $q''=54.3 \text{ kW/m}^2$ and (b) R1233zd(E), $T_{sat}=94.8^\circ\text{C}$, $q''=54.3 \text{ kW/m}^2$ (I: Intermittent flow, A: Annular flow, D: Dryout).

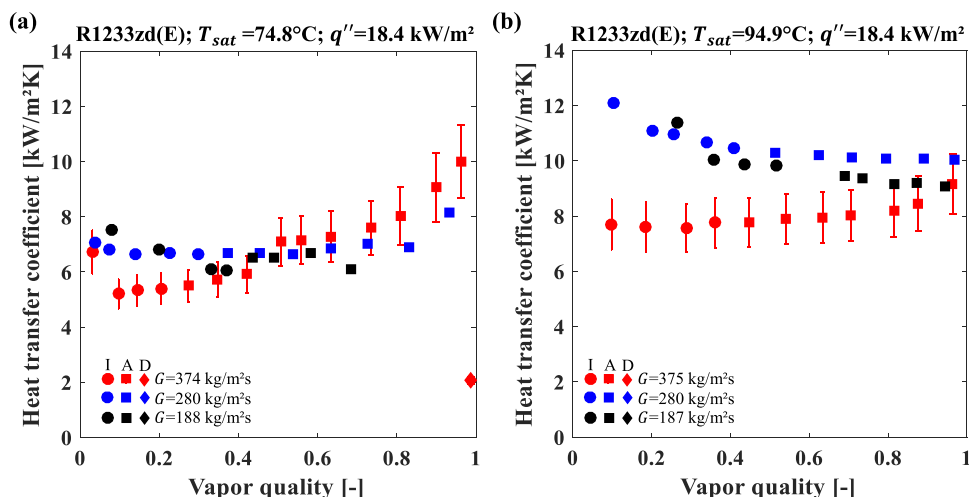


Fig. 15. Mass velocity effect on the heat transfer coefficient for (a) R1233zd(E), $T_{sat}=74.8^\circ\text{C}$, $q''=18.4 \text{ kW/m}^2$ and (b) R1233zd(E), $T_{sat}=94.9^\circ\text{C}$, $q''=18.4 \text{ kW/m}^2$ (I: Intermittent flow, A: Annular flow, D: Dryout).

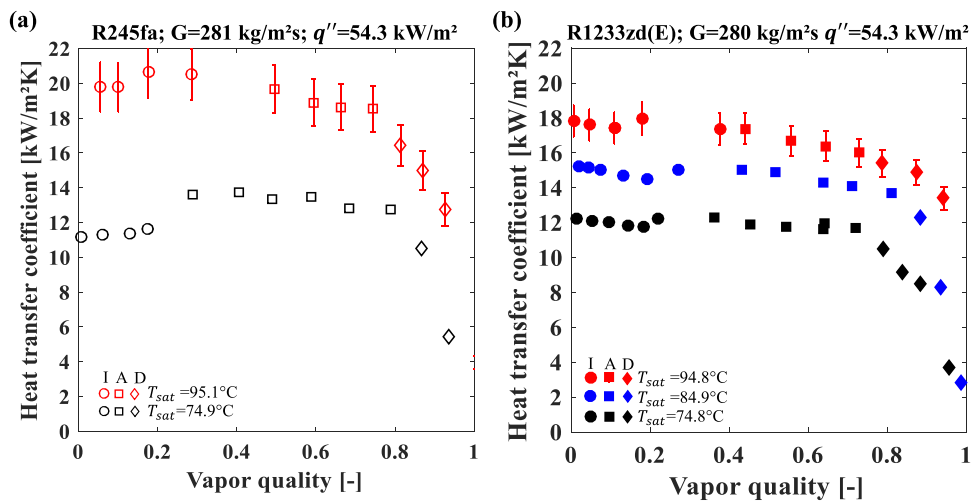


Fig. 16. Saturation temperature effect on the heat transfer coefficient for (a) R245fa, $G = 281 \text{ kg/m}^2\text{s}$, $q'' = 54.3 \text{ kW/m}^2$ and (b) R1233zd(E), $G = 280 \text{ kg/m}^2\text{s}$, $q'' = 54.3 \text{ kW/m}^2$ (I: Intermittent flow, A: Annular flow, D: Dryout).

reduction with increasing vapor quality at low x , which is associated with the increase of flow velocity and larger temperature gradients along the liquid phase near the heated surface. At intermediate and high x , annular flow pattern prevails, however, the experimental results indicate that nucleate boiling still plays a relevant role in the heat transfer, since the HTC remained almost invariable until the dryout, when a sudden drop in its value is displayed in Fig. 13. The strong bubble nucleation activity even during annular flow was previously confirmed by Layssac et al. [25] through the visualization of R245fa flow boiling at $T_{sat}=81^\circ\text{C}$ in a 1.6 mm diameter sapphire ITO-coated tube. Different from most of experimental results obtained in the present study, the HTC data reported in Fig. 13a at $q''=18.4 \text{ kW/m}^2$ show an increasing behavior for vapor qualities higher than 0.1. Such a behavior suggests a significant contribution of convective effects to the heat transfer, which might be associated with the lower saturation temperature and heat flux of these data.

The mass velocity effect on the heat transfer coefficient is illustrated in Figs. 14 and 15. For a higher heat flux (Fig. 14) a higher wall temperature is expected compared to a lower heat flux (Fig. 15). Therefore, it can be speculated that a much broader range of cavity sizes are activated for the highest heat flux, including the smaller ones. Under this condition, it is supposed that the liquid temperature gradient near the wall is enough to maintain a sufficiently high number of active nucleation sites, significantly decreasing the impact of the two-phase flow velocity on the heat transfer coefficient. However, it is important to highlight that nucleation suppression effects seem to be also displayed in Fig. 14(b) for vapor qualities in between 0.2 and 0.3. Despite the differences in the HTC being within the uncertainty of HTC measurements, such a behavior can be characterized by a local heat transfer coefficient minimum. The slight increase of the HTC with x for vapor quality higher than this minimum seems associated to the enhancement of convective effects. Besides, slightly higher HTC for the highest mass velocity for vapor qualities lower than 0.8 also corroborates the occurrence of some influence of convective effects on the HTC, independently of the vapor quality range.

The data presented in Fig. 15 concerns a heat flux about 1/3 of the heat flux of the data displayed in Fig. 14. Therefore, a much lower number of active nucleation sites are expected to occur. Besides, it is not expected that the smaller cavities are activated under the lowest heat flux conditions due to the lower wall temperature. Both behaviors favor the suppression of bubble nucleation and the predominance of convective effects over nucleate boiling effects on the heat transfer coefficient. In Fig. 15, for low vapor qualities, nucleate boiling suppression is characterized by a lower HTC for the highest mass velocity independently of

the saturation temperature. In the case of Fig. 15b, nucleate boiling suppression seems associated with the increase of the two-phase velocity with liquid evaporation for mass velocities of 187 and 280 kg/m²s, while for the highest mass velocity the enhancement of convective effects due to increment of vapor quality seems to counterbalance the reduction of nucleate boiling effects due to its suppression, maintaining the HTC almost constant over all the vapor quality range. Under the condition of the lowest saturation temperature and lowest heat flux (Fig. 15a), the contribution of nucleate boiling effects to the HTC is reduced if compared to convective effects. Except for dryout conditions and vapor qualities lower than 0.3, it implies the increase of the heat transfer coefficient with vapor quality due to the enhancement of convective effects independently of the mass velocity.

It is important to highlight that the discussions on the HTC behaviors displayed in Fig. 14 and 15 are based on hypotheses built by the authors based on their own knowledge and previous literature. Therefore, further studies on the boiling fundamental aspects under conditions of high reduced pressures are suggested here. These investigations should be based on simultaneous images of the wall temperature field, through high-speed IR thermography, and of the two-phase flow, through high-speed videos in order to characterize bubbles frequency and their departure diameter, transient conduction in the heated wall, nucleation active site density, entrainment, the wet and dry portions of the heated surface and liquid film thickness for annular flow. Only based on these results, it will be possible to characterize the mechanisms associated to the behaviors and validate them.

In addition, it seems that the increase of the mass velocity postpones the dryout incipience to higher vapor qualities. A similar effect was recently verified by Zhao et al. [81] for R1233zd(E), R245fa, R1224yd and HFE347pc-f flow boiling at saturation temperatures up to 70 °C. According to Morse et al. [82] and Bapstilletta et al. [83], dryout is associated with the frequency of the intermittent surface dryout and its rewetting caused by liquid fronts within the liquid film. In this context, it is plausible that the inertia of these liquid fronts increases with increasing mass velocity, postponing the dryout. Comparing Figs. 14b and 15b also indicates the postponement of the liquid film dryout with reducing q'' , a behavior typically verified in the literature for both low [82] and high T_{sat} [20, 26, 36, 37].

Fig. 16 displays the effect of the saturation temperature on the HTC and the corresponding flow pattern of each datapoint. According to this figure, the higher the saturation temperature, the greater the heat transfer coefficient, regardless of the vapor quality range. Increasing T_{sat} implies on reducing surface tension and enthalpy of vaporization (see Table 2), and, consequently, minimizing the wall superheating

Table 6

Mean average errors resulting of the comparison between the heat transfer coefficient database obtained in the present study and prediction methods.

| Authors | MAE (%) | | | Experimental conditions covered by the database used to the development of the method |
|---|----------|--------|-------------|---|
| | All data | R245fa | R1233zd (E) | |
| <i>Empirical correlations</i> | | | | |
| Tran et al. [47] | 32.6 | 26.8 | 34.1 | C,R/S/H; R12, R113; D_H : 2.4–2.92 mm; p_r : 0.045–0.20; G: 44–832 kg/m ² ; q^* : 3.6–129 kW/m ² ; 296 data points |
| Kew and Cornwell [86] | 36.8 | 36.2 | 36.9 | C,R/S/H; R141b; D_H : 1.39–3.69 mm; 697 data points |
| Sun and Mishima [87] | 33.5 | 37.8 | 32.5 | C,R,S,M/H,V; R11, R12, R123, R134a, R141b, R22, R404A, R407C, R410A, CO ₂ , water; D_H : 0.21–6.5 mm; p_r : 0.005–0.61; G: 44–1500 kg/m ² ; q^* : 5–109 kW/m ² ; 2505 data points |
| Shen et al. [85] | 40.8 | 12.7 | 47.7 | C/S/V; Water; D_H : 19 mm; p_r : 0.5–0.97; G: 170–800 kg/m ² ; q^* : 85–505 kW/m ² |
| <i>Based on superposition of effects</i> | | | | |
| Gungor and Winterton [50] | 25.6 | 23.7 | 26.0 | C,A/S/H,V; Water, R11, R12, R22, R113, R114, ethylene-glycol, D_H : 2.95 mm; p_r : 0.002–0.91; G: 21–61,518 kg/m ² ; q^* : 0.35–91,534 kW/m ² ; 4300 data points |
| Jung et al. [88] | 39.7 | 37.0 | 40.3 | C/S/H; R12, R152a, R22, R114, R500; D_H : 9 mm; p_r : 0.08; G: 250–720 kg/m ² ; q^* : 10–45 kW/m ² ; 1588 data points |
| Yun et al. [89] | 33.8 | 24.1 | 36.1 | C/S/H; CO ₂ ; D_H : 0.79–2 mm; p_r : 0.47–0.87; G: 190–3571 kg/m ² ; q^* : 5–48.1 kW/m ² ; 741 data points |
| Choi et al. [46] | 32.7 | 28.6 | 33.7 | C/S/H; CO ₂ ; D_H : 1.5–3 mm; p_r : 0.36–0.61; G: 200–600 kg/m ² ; q^* : 20–40 kW/m ² ; 471 data points |
| Ozawa et al. [90] | 24.1 | 25.6 | 23.7 | C/S/H; CO ₂ ; D_H : 2 mm; p_r : 0.68–0.91; G: 200–500 kg/m ² ; q^* : 5–35 kW/m ² |
| Del Col [91] | 37.1 | 36.1 | 37.3 | C/S/H; R134a, R22, R125, R410A; D_H : 8 mm; p_r : 0.19–0.53; G: 200–600 kg/m ² ; q^* : 9–53 kW/m ² ; 108 data points |
| Ducoulombier et al. [92] | 18.9 | 19.0 | 18.9 | C/S/H; CO ₂ ; D_H : 0.529 mm; p_r : 0.36–0.47; G: 200–1200 kg/m ² ; q^* : 10–30 kW/m ² ; 2710 data points |
| Kim and Mudawar [93] | 38.4 | 34.2 | 39.4 | C,R,S,M/H,V; FC72, R11, R113, R123, R1234yf, R1234ze, R134a, R152a, R22, R236fa, R245fa, R32, R404A, R407C, R410A, R417A, CO ₂ , water; D_H : 0.19–6.5 mm; p_r : 0.005–0.69; G: 19–1608 kg/m ² ; 10,805 data points |
| Kanizawa et al. [84] | 38.1 | 28.4 | 40.4 | C/S/H; R134a, R245fa, R600a; D_H : 0.38–2.6 mm; p_r : 0.04–0.27; G: 49–2200 kg/m ² ; q^* : 5–185 kW/m ² ; 2047 data points |
| Billiet et al. [23] | 35.5 | 33.0 | 36.1 | C/S/H; R245fa; D_H : 3 mm; p_r : 0.07–0.58; G: 100–1000 kg/m ² ; q^* : 10–50 kW/m ² |
| Wang et al. [27] | 18.2 | 16.9 | 18.5 | C/S/H; R245fa; D_H : 10 mm; p_r : 0.07–0.13; G: 193–386 kg/m ² ; q^* : 10–36 kW/m ² ; data points |
| Luo et al. [35] | 26.0 | 24.1 | 26.5 | C/S/H; R245fa; D_H : 10 mm; p_r : 0.22–0.48; G: 248–460 kg/m ² ; 147 data points |

A: Annular; C: Circular; R: Rectangular; F: Flattened; T: Triangular; S: Single-channel; M: Multi-channels; H: Horizontal; V: Vertical.

necessary to trigger the nucleation of vapor bubbles. Therefore, the nucleation sites density increases and nucleate boiling effects are enhanced. It is important to remark that, although the HTC increment with increasing T_{sat} was verified along the entire range of vapor qualities, this effect is more pronounced under low x conditions. In general, the increase of T_{sat} anticipated the liquid film dryout, which is a consequence of the stronger nucleation activity.

7.2. Heat transfer coefficient prediction methods evaluation

In this subitem, the experimental results corresponding to conditions prior the dryout are compared against sixteen prediction methods for the heat transfer coefficient through the convective boiling mechanism. In this analysis, the methods were classified as empirical and based on the superposition of nucleate boiling and convective effects. Table 6 presents the experimental conditions for which these methods were developed, and the statistical results obtained from the comparisons. The most significant differences between the MAEs obtained for the refrigerants R245fa and R1233zd(E) were verified for the methods of Kanizawa et al. [84] and Shen et al. [85], 12.0% and 34.9%, respectively. The database used by Kanizawa et al. [84] to develop their method included experimental results for R245fa at $T_{sat}=25.5$ –58.3 °C, but not for R1233zd(E). Although thermophysical properties of water are considerably different from those of organic refrigerants, curiously, the method proposed by Shen et al. [85], developed exclusively for water flow boiling at high reduced pressures ($p_r=0.5$ –0.97), presented the lowest MAE for R245fa among all the methods evaluated, 12.7%.

Mean average errors lower than 26% were provided by the prediction method originally developed by Gungor and Winterton [50], and its modified versions recently proposed by Wang et al. [27] and Luo et al. [35]. The lowest mean average error was provided by the method of Wang et al. [27], predicting 83.3% of the datapoints within a ±30% error band. These authors modified the nucleate boiling effects enhancement factor originally proposed by Gungor and Winterton [50], in order to predict their R245fa flow boiling data at $T_{sat}=40$ –60 °C. According to Luo et al. [35], the method of Gungor and Winterton [50] underestimated the contribution of nucleate boiling effects at high mass

velocities and the effects of increasing evaporation temperature on the convective contribution to the HTC. In order to capture such effects, Luo et al. [35] modified the original method of Gungor and Winterton [50] by adjusting new exponents to the boiling number and the Lockhart-Martinelli parameter, predicting 95% of their database for R245fa ($T_{sat}=80$ –150 °C) within an error band of ±30%.

Reasonably accurate predictions were also provided by the methods proposed exclusively for CO₂ [46,90,92]. The reasonable agreement between the present database and these methods might be associated with the high reduced pressures of the CO₂ experimental results included in the databases ($p_r=0.36$ –0.87) used in their development. It allows the methods to capture the strong contribution of nucleate boiling effects to the heat transfer as show by the data obtained in the present study. The accuracy of CO₂-based prediction methods for R245fa at high saturation temperatures was previously pointed out by Charnay et al. [21]. According to these authors, the method of Choi et al. [46] predicted 88.8% of their database within a ±30% error band and provided the lowest MAE of 16.7%, being the most accurate among the methods evaluated by them.

Fig. 17 presents the comparison between experimental data and the corresponding predictions of the six methods that provided the lowest mean average errors. A general trend of underprediction of experimental data is verified in Fig. 17 for the methods of Gungor and Winterton [50] Choi et al. [46], Wang et al. [27] and Luo et al. [35], especially for the results obtained at $T_{sat}=95$ °C, which usually presented higher deviations. On the other hand, the methods proposed by Ozawa et al. [90] and Ducoulombier et al. [92] overestimated a significant parcel of the database and presented their highest accuracy for $T_{sat}=95$ °C.

Fig. 18 presents a comparison of the HTC trends with vapor quality between the experimental data and the prediction methods found as the most accurate in the present study. In general, the data at $T_{sat}=74.8$ °C (Figs. 18a, 18c and 18d) was reasonably predicted by the methods of Gungor and Winterton [50], Luo et al. [35] and, especially, Wang et al. [27]. However, as previously mentioned, the data are significantly underpredicted by these methods at $T_{sat}=94.9$ °C (Fig. 18b). The methods of Choi et al. [46] and Ducoulombier et al. [92] presented HTC increasing behavior with increasing x , which, in the present study, was

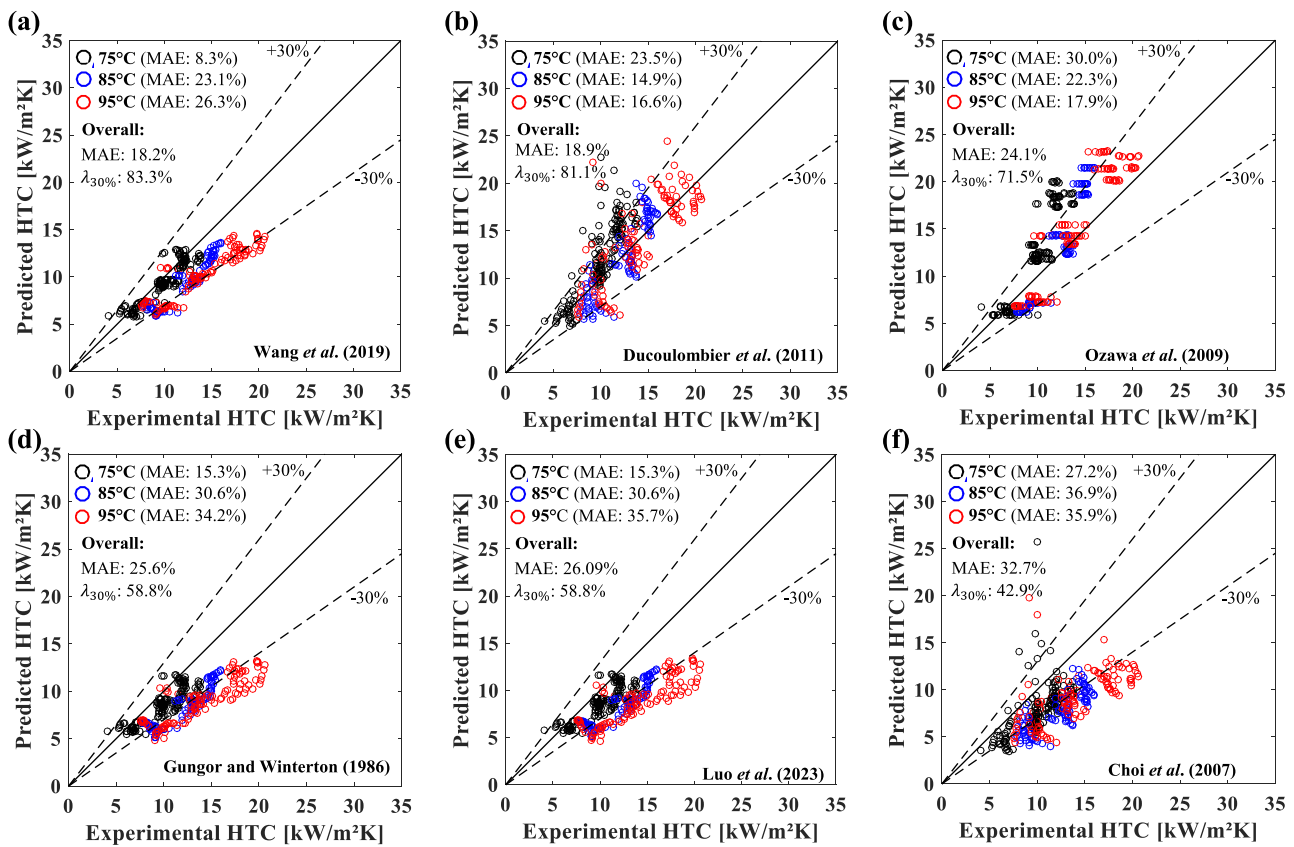


Fig. 17. Comparison between experimental heat transfer coefficient and predictions according to (a) Wang et al. [27], (b) Ducoulombier et al. [92], (c) Ozawa et al. [90], (d) Gungor and Winterton [50], (e) Luo et al. [35] and (f) Choi et al. [46].

only verified at low q'' and high G . The method proposed by Ozawa et al. [90] does not consider HTC variations with increasing x and has satisfactorily captured the HTC trend at $T_{sat}=94.9$ °C (Fig. 18b). This method presents a strong sensitivity to heat flux variations, which is confirmed by comparing Figs. 18c and 18d. All the experimental data corresponding to the highest heat flux evaluated were overpredicted by the correlation of Ozawa et al. [90], as depicted in Fig. 18d.

8. Conclusions

Based on the experimental results obtained in the present study, the following main conclusions can be drawn:

- Based on two-phase flow images flow patterns were classified as intermittent and annular. The onset of liquid film dryout was identified through the HTC measurements. As well as verified in low temperature experiments, the intermittent-annular transition was anticipated with increasing the mass velocity and reducing the saturation temperature. In general, the onset of liquid film dryout was anticipated with increasing q'' and T_{sat} , and reducing G . In addition, stratification effects were verified despite of the small diameter of the test section;
- As expected, the frictional pressure gradient decreases as the saturation temperature increases and mass velocity decreases. Based on the analysis of two-phase flow images, it was possible to conclude that the shift in the trend of the pressure gradient at high vapor qualities, characterized by a maximum pressure gradient, is associated with the damping of disturbance waves at the liquid-vapor interface;
- In general, the experimental results for the heat transfer coefficient indicated the predominance of nucleate boiling effects, with its

relative importance presenting a slight reduction as the vapor quality increases. This conclusion is corroborated by the fact that the higher the heat flux and saturation temperature, the higher was the heat transfer coefficient independent of the vapor qualities range. As typically verified for nucleate boiling dominated heat transfer, the mass velocity increase reduced the HTC or, for most of the data presented non-relevant effect. However, for some experimental results at low saturation temperatures and heat fluxes, higher HTCs were verified at intermediate-to-high vapor qualities for high mass velocities, indicating convective effects dominance;

- The methods proposed by Nie et al. [77] and Muller-Steinhagen and Heck [43] performed as the best ones predicting more than 90% of the pressure drop data obtained in the present study within a $\pm 30\%$ error band. In addition, these methods were equally accurate independent of the saturation temperature. It was also verified that 7 of the 9 homogeneous-based methods presented progressive reduction of the MAE with increasing the saturation temperature;
- In general, the prediction methods for the HTC underestimated the experimental data, especially under conditions of higher saturation temperatures. The method proposed by Gungor and Winterton [50] and its modifications recently proposed by Luo et al. [35] and Wang et al. [27] presented reasonably accuracy, especially the last one, which predicted more than 80% of the experimental data within a $\pm 30\%$ error band. Methods exclusively developed for CO₂ also provided accurate predictions of the present database, especially at high T_{sat} . Despite the low saturation temperature of the CO₂ data considered in the development of these methods, the low critical temperature of this fluid leads to intermediate-to-high reduced pressures. It allows the CO₂ methods to capture the strong contribution of nucleate boiling effects typically verified in the present study.

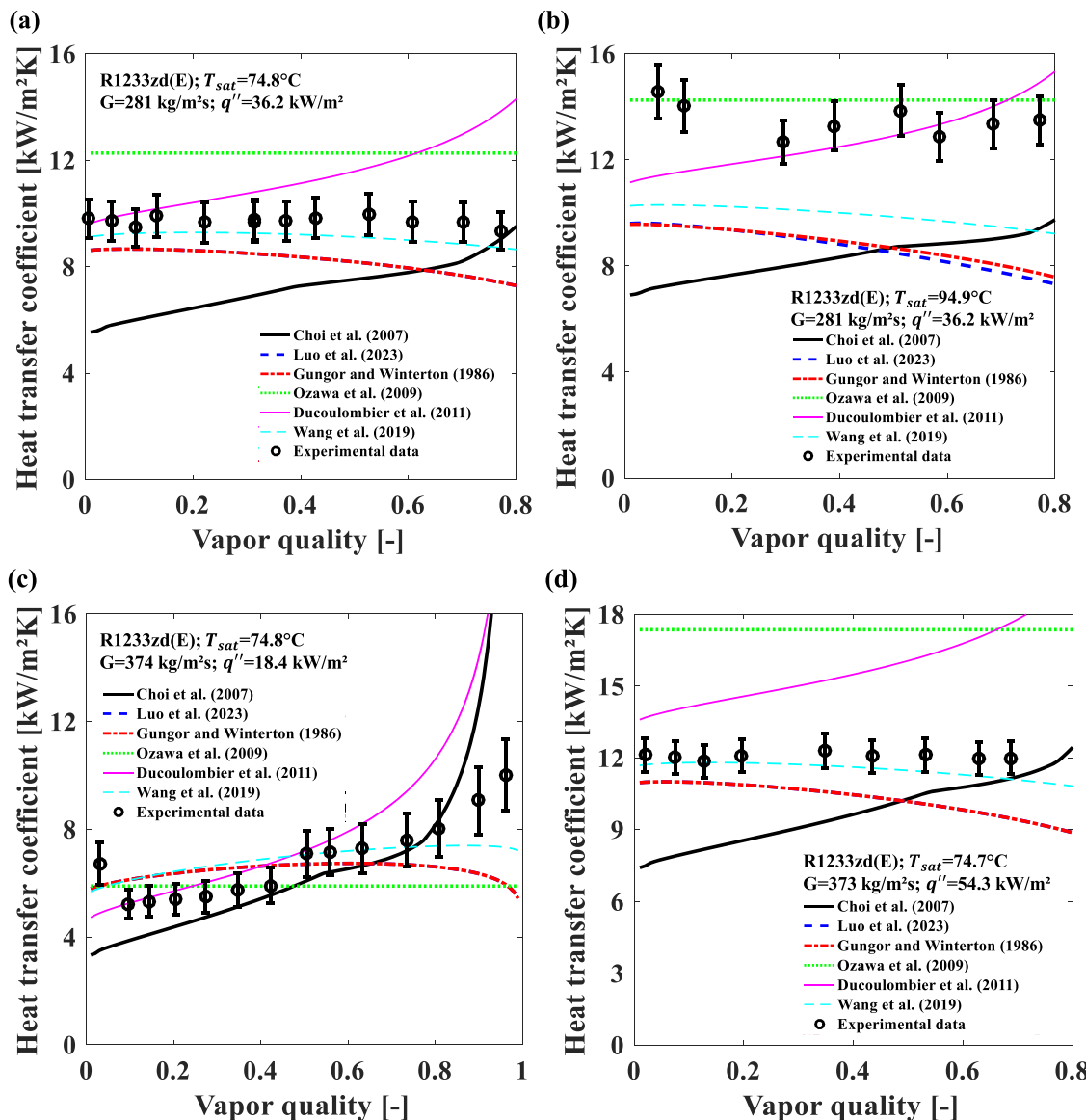


Fig. 18. Comparison between experimental data and heat transfer coefficient prediction methods. (a) R1233zd(E), $T_{sat}=74.8^{\circ}\text{C}$, $G=281 \text{ kg/m}^2\text{s}$, $q''=36.2 \text{ kW/m}^2$; (b) R1233zd(E), $T_{sat}=94.9^{\circ}\text{C}$, $G=281 \text{ kg/m}^2\text{s}$, $q''=36.2 \text{ kW/m}^2$; (c) R1233zd(E), $T_{sat}=74.8^{\circ}\text{C}$, $G=374 \text{ kg/m}^2\text{s}$, $q''=18.4 \text{ kW/m}^2$; (d) R1233zd(E), $T_{sat}=74.7^{\circ}\text{C}$, $G=373 \text{ kg/m}^2\text{s}$, $q''=54.3 \text{ kW/m}^2$.

Declaration of Competing Interest

The authors declare the following financial interests/personal relationships which may be considered as potential competing interests:

Daniel Borba Marchetto reports financial support was provided by State of São Paulo Research Foundation. Gherhardt Ribatski reports financial support was provided by State of São Paulo Research Foundation.

Data availability

Data will be made available on request.

Acknowledgments

The authors gratefully acknowledge the São Paulo Research Foundation (FAPESP, Brazil) for the scholarships given to the first author, under Contract Numbers 2019/22105–5 and 2020/06705–0. The

authors also acknowledge the support through the Thematic Grant provided by FAPESP under Contract Number 2016/09509–01. The authors also acknowledge Mr. Christophe Ducat, Mr. Nicolas Pouchot, Mr. Antoine Berlandi and Mr. Xavier Durand for the technical support on the development of the experimental apparatus, Mr. Bernard Lacroix, Mr. Anthony Buthod, Mr. Serge Buathier and Mr. Jorge Nicolau dos Santos for the data acquisition setup development.

References

- [1] M.A. Qyyum, A. Khan, S. Ali, M.S. Khurram, N. Mao, A. Naquash, A.A. Noon, T. He, M. Lee, Assessment of working fluids, thermal resources and cooling utilities for Organic Rankine Cycles: state-of-the-art comparison, challenges, commercial status, and future prospects, Energy Convers. Manag. 252 (2022) 115055, <https://doi.org/10.1016/j.enconman.2021.115055>.
- [2] W. Chen, W. Geng, Fossil energy saving and CO₂ emissions reduction performance, and dynamic change in performance considering renewable energy input, Energy 120 (2017) 283–292, <https://doi.org/10.1016/j.energy.2016.11.080>.
- [3] K. Rahbar, S. Mahmoud, R.K. Al-Dadah, N. Moazami, S.A. Mirhadizadeh, Review of organic Rankine cycle for small-scale applications, Energy Convers. Manag. 134 (2017) 135–155, <https://doi.org/10.1016/j.enconman.2016.12.023>.

- [4] Y. Zhu, W. Li, Y. Wang, H. Li, S. Li, Thermodynamic analysis and parametric optimization of ejector heat pump integrated with organic Rankine cycle combined cooling, heating and power system using zeotropic mixtures, *Appl. Therm. Eng.* 194 (2021), 117097, <https://doi.org/10.1016/j.applthermaleng.2021.117097>.
- [5] M.M. Marinheiro, G.M. Coraça, L. Cabezas-Gomez, G. Ribatski, Detailed transient assessment of a small-scale concentrated solar power plant based on the organic Rankine cycle, *Appl. Therm. Eng.* 204 (2022), 117959, <https://doi.org/10.1016/j.applthermaleng.2021.117959>.
- [6] C. Arpagaus, F. Bless, M. Uhlmann, J. Schiffmann, S.S. Bertsch, High temperature heat pumps: market overview, state of the art, research status, refrigerants, and application potentials, *Energy* 152 (2018) 985–1010, <https://doi.org/10.1016/j.energy.2018.03.166>.
- [7] C. Mateu-Royo, S. Sawalha, A. Mota-Babiloni, J. Navarro-Esbrí, High temperature heat pump integration into district heating network, *Energy Convers. Manag.* 210 (2020), 112719, <https://doi.org/10.1016/j.enconman.2020.112719>.
- [8] B. Eppinger, D. Steger, C. Regensburger, J. Karl, E. Schläcker, S. Will, Carnot battery: simulation and design of a reversible heat pump-organic Rankine cycle pilot plant, *Appl. Energy* 15 (2021), 116650, <https://doi.org/10.1016/j.apenergy.2021.116650>.
- [9] Y. Zhang, R. Tian, X. Dai, D. Wang, Y. Ma, H. Li, L. Shi, Experimental study of R134a flow boiling in a horizontal tube for evaporator design under typical Organic Rankine Cycle pressures, *Int. J. Heat Fluid Flow* 71 (2018) 210–219, <https://doi.org/10.1016/j.ijheatfluidflow.2018.04.00>.
- [10] C. He, C. Liu, H. Gao, H. Xie, Y. Li, S. Wu, J. Xu, The optimal evaporation temperature and working fluids for subcritical organic Rankine cycle, *Energy* 38 (2012) 136–143, <https://doi.org/10.1016/j.energy.2011.12.022>.
- [11] W. Su, L. Zhao, S. Deng, Simultaneous working fluids design and cycle optimization for Organic Rankine cycle using group contribution model, *Appl. Energy* 202 (2017) 618–627, <https://doi.org/10.1016/j.apenergy.2017.03.133>.
- [12] A.F. Babatunde, O.O. Sunday, A review of working fluids for organic Rankine cycle (ORC) applications, in: Proceedings of the IOP Conference Series: Materials Science And Engineering 413, IOP Publishing, 2018, 012019, <https://doi.org/10.1088/1757-899X/413/1/012019>.
- [13] D.B. Marchetto, D.C. Moreira, R. Revellin, G. Ribatski, A state-of-the-art review on flow boiling at high reduced pressures, *Int. J. Heat Mass Transf.* 193 (2022), 122951, <https://doi.org/10.1016/j.ijheatmasstransfer.2022.122951>.
- [14] M. Zhang, R.L. Webb, Correlation of two-phase friction for refrigerants in small-diameter tubes, *Exp. Therm. Fluid Sci.* 25 (2001) 131–139, [https://doi.org/10.1016/S0894-1777\(01\)00066-8](https://doi.org/10.1016/S0894-1777(01)00066-8).
- [15] P. Vassallo, K. Keller, Two-phase frictional pressure drop multipliers for SUVA R-134a flowing in a rectangular duct, *Int. J. Multipiph. Flow* 32 (2006) 466–482, <https://doi.org/10.1016/j.ijmultiphaseflow.2006.01.00>.
- [16] B.R. Vijayarangan, S. Jayanti, A.R. Balakrishnan, Pressure drop studies on two-phase flow in a uniformly heated vertical tube at pressures up to the critical point, *Int. J. Heat Mass Transf.* 50 (2007) 1879–1891, <https://doi.org/10.1016/j.ijheatmasstransfer.2006.10>.
- [17] E. Costa-Patry, J. Olivier, J. Thome, Heat transfer characteristics in a copper micro-evaporator and flow pattern-based prediction method for flow boiling in microchannels, *Front. Heat Mass Transf.* 3 (2012), 013002, <https://doi.org/10.5098/hmt.v3.i1.3002>.
- [18] R. Charnay, R. Revellin, J. Bonjour, Flow boiling characteristics of R-245fa in a minichannel at medium saturation temperatures, *Exp. Therm. Fluid Sci.* 59 (2014) 184–194, <https://doi.org/10.1016/j.expthermflusci.2014.01.011>.
- [19] R. Charnay, R. Revellin, J. Bonjour, Discussion on the validity of prediction tools for two-phase flow pressure drops from experimental data obtained at high saturation temperatures, *Int. J. Refrig.* 54 (2015) 98–125, <https://doi.org/10.1016/j.ijrefrig.2015.02.014>.
- [20] R. Charnay, R. Revellin, J. Bonjour, Flow boiling heat transfer in minichannels at high saturation temperatures: part I—Experimental investigation and analysis of the heat transfer mechanisms, *Int. J. Heat Mass Transf.* 87 (2015) 636–652, <https://doi.org/10.1016/j.ijheatmasstransfer.2015.03.081>.
- [21] R. Charnay, R. Revellin, J. Bonjour, Flow boiling heat transfer in minichannels at high saturation temperatures: part II—Assessment of predictive methods and impact of flow regimes, *Int. J. Heat Mass Transf.* 87 (2015) 653–672, <https://doi.org/10.1016/j.ijheatmasstransfer.2015.03.080>.
- [22] T. Mawatari, H. Mori, An experimental study on characteristics of post-CHF heat transfer in the high subcritical pressure region near to the critical pressure, *J. Therm. Sci. Technol.* 11 (2016) JTST0006, <https://doi.org/10.1299/jst.2016jst0006>. -JTST0006.
- [23] M. Billiet, B. Ameel, R. Charnay, R. Revellin, M. De Paeppe, Flow regime based heat transfer correlation for R245fa in a 3mm tube, *Int. J. Heat Mass Transf.* 117 (2018) 1304–1311, <https://doi.org/10.1016/j.ijheatmasstransfer.2017.10.062>.
- [24] T. Layssac, S. Lips, R. Revellin, Experimental study of flow boiling in an inclined mini-channel: effect of inclination on flow pattern transitions and pressure drops, *Exp. Therm. Fluid Sci.* 98 (2018) 621–633, <https://doi.org/10.1016/j.expthermflusci.2018.07.004>.
- [25] T. Layssac, S. Lips, R. Revellin, Effect of inclination on heat transfer coefficient during flow boiling in a mini-channel, *Int. J. Heat Mass Transf.* 132 (2019) 508–518, <https://doi.org/10.1016/j.ijheatmasstransfer.2018.12.001>.
- [26] G. Lillo, R. Mastrullo, A.W. Mauro, L. Viscito, Flow boiling of R1233zd (E) in a horizontal tube: experiments, assessment and correlation for asymmetric annular flow, *Int. J. Heat Mass Transf.* 129 (2019) 547–561, <https://doi.org/10.1016/j.ijheatmasstransfer.2018.09.117>.
- [27] D. Wang, L. Zhao, X. Nie, Y. Lu, S. Deng, Experimental study on flow boiling characteristics of R-245fa in circular tube under non-uniform heat flux, *Int. J. Heat Mass Transf.* 143 (2019), 118570.
- [28] Q. Guo, M. Li, X. Tian, Experimental study on flow boiling heat transfer characteristics of R134a, R245fa and R134a/R245fa mixture at high saturation temperatures, *Int. J. Therm. Sci.* 150 (2020), 106195, <https://doi.org/10.1016/j.ijthermalsci.2019.106195>.
- [29] A. Zhao, Y. Fan, Y. Suzuki, K. Morimoto, Flow boiling heat transfer of low-GWP working fluids at low mass and heat fluxes in a 4mm diameter tube, *Int. J. Heat Mass Transf.* 162 (2020), 120332, <https://doi.org/10.1016/j.ijheatmasstransfer.2020.120>.
- [30] X.Y. You, J.H. Liu, N. Hua, J. Wang, R.J. Xu, G.X. Yu, H.S. Wang, Experimental study on flow boiling of refrigerant R1233zd (E) in microchannels: heat transfer, *Appl. Therm. Eng.* 182 (2021), 116083, <https://doi.org/10.1016/j.applthermaleng.2020.116083>.
- [31] A. Arcasi, R. Mastrullo, A.W. Mauro, L. Viscito, Adiabatic frictional pressure gradient during flow boiling of pure refrigerant R1233zd and non-azeotropic mixtures R448A, R452A and R455A, *Journal of Physics: Conference Series* 2177 (2022), 012045, <https://doi.org/10.1088/1742-6596/2177/1/012045>.
- [32] S. Halon, Z. Krolicki, R. Revellin, B. Zajaczkowski, Heat transfer characteristics of flow boiling in a micro channel array with various inlet geometries, *Int. J. Heat Mass Transf.* 187 (2022), 122549, <https://doi.org/10.1016/j.ijheatmasstransfer.2022.122549>.
- [33] A. Kaya, S. Lecompte, M. De Paeppe, Experimental flow boiling study of R245a at high reduced pressures in a large diameter horizontal tube, *Energies* 15 (2022) 864, <https://doi.org/10.3390/en15030864>.
- [34] H. Li, P. Hrnjak, Heat transfer coefficient, pressure gradient, and flow patterns of R1233zd (E) and R1336mzz (Z) evaporating in a microchannel tube, *Int. J. Heat Mass Transf.* 182 (2022), 121992, <https://doi.org/10.1016/j.ijheatmasstransfer.2021.121992>.
- [35] X. Luo, Y. Xia, J. Huang, J. He, J. Tu, J. Chen, Y. Liang, Z. Yang, Y. Chen, Experimental investigation on high-temperature flow boiling heat transfer characteristics of R245fa in a horizontal circular tube, *Appl. Therm. Eng.* 225 (2023), 120260, <https://doi.org/10.1016/j.applthermaleng.2023.120260>.
- [36] M. Pysz, S. Gluch, D. Mikielewicz, Experimental study of flow boiling pressure drop and heat transfer of R1233zd (E) at moderate and high saturation temperatures, *Int. J. Heat Mass Transf.* 204 (2023), 123855, <https://doi.org/10.1016/j.ijheatmasstransfer.2023.123855>.
- [37] M. Pysz, D. Mikielewicz, Flow boiling of R1233zd (E) in a 3mm vertical tube at moderate and high reduced pressures, *Exp. Therm. Fluid Sci.* 147 (2023), 110964, <https://doi.org/10.1016/j.expthermflusci.2023.110964>.
- [38] J. Zhang, F. Haglind, Experimental analysis of high temperature flow boiling heat transfer and pressure drop in a plate heat exchanger, *Appl. Therm. Eng.* 196 (2021), 117269.
- [39] A. Desideri, J. Zhang, M.R. Kærn, T.S. Ommen, J. Wronski, V. Lemort, F. Haglind, An experimental analysis of flow boiling and pressure drop in a brazed plate heat exchanger for organic Rankine cycle power systems, *Int. J. Heat Mass Transf.* 113 (2017) 6–21, <https://doi.org/10.1016/j.ijheatmasstransfer.2017.05.063>.
- [40] J. Zhang, A. Desideri, M.R. Kærn, T.S. Ommen, J. Wronski, F. Haglind, Flow boiling heat transfer and pressure drop characteristics of R134a, R1234yf and R1234ze in a plate heat exchanger for organic Rankine cycle units, *Int. J. Heat Mass Transf.* 108 (2017) 1787–1801, <https://doi.org/10.1016/j.applthermaleng.2021.1172>.
- [41] L. Friedel, Improved friction pressure drop correlation for horizontal and vertical two-phase pipe flow. Proceedings of the European Two-Phase Flow Group Meet, Ispra, Italy, 1979.
- [42] D. Chisholm, Pressure gradients due to friction during the flow of evaporating two-phase mixtures in smooth tubes and channels, *Int. J. Heat Mass Transf.* 16 (1973) 347–358, [https://doi.org/10.1016/0017-9310\(73\)90063-X](https://doi.org/10.1016/0017-9310(73)90063-X).
- [43] H. Müller-Steinhagen, K. Heck, A simple friction pressure drop correlation for two-phase flow in pipes, *Chem. Eng. Process. Process Intensif.* 20 (1986) 297–308, [https://doi.org/10.1016/0255-2701\(86\)80008-3](https://doi.org/10.1016/0255-2701(86)80008-3).
- [44] D.H. Beggs, J.P. Brill, A study of two-phase flow in inclined pipes, *J. Petrol. Technol.* 25 (1973) 607–617, <https://doi.org/10.2118/4007-PA>.
- [45] Y.W. Hwang, M.S. Kim, The pressure drop in microtubes and the correlation development, *Int. J. Heat Mass Transf.* 49 (2006) 1804–1812, <https://doi.org/10.1016/j.ijheatmasstransfer.2005.10.040>.
- [46] K.I. Choi, A.S. Pamitran, J.T. Oh, Two-phase flow heat transfer of CO₂ vaporization in smooth horizontal minichannels, *Int. J. Refrig.* 30 (2007) 767–777, <https://doi.org/10.1016/j.ijrefrig.2006.12.006>.
- [47] T.N. Tran, M.W. Wambagsans, D.M. France, Small circular-and rectangular-channel boiling with two refrigerants, *Int. J. Multipiph. Flow* 22 (1996) 485–498, [https://doi.org/10.1016/0301-9322\(96\)00002-X](https://doi.org/10.1016/0301-9322(96)00002-X).
- [48] P. Thiangtham, C. Keeplaiboon, P. Kiatpachai, L.G. Asirvatham, O. Mahian, A. S. Dalkilic, S. Wongwises, An experimental study on two-phase flow patterns and heat transfer characteristics during boiling of R134a flowing through a multi-microchannel heat sink, *Int. J. Heat Mass Transf.* 98 (2016) 390–400, <https://doi.org/10.1016/j.ijheatmasstransfer.2016.02.002>.
- [49] S.S. Bertsch, E.A. Groll, S.V. Garimella, Effects of heat flux, mass flux, vapor quality, and saturation temperature on flow boiling heat transfer in microchannels, *Int. J. Multipiph. Flow* 35 (2009) 142–154, <https://doi.org/10.1016/j.ijmultiphaseflow.2008.10.004>.
- [50] K.E. Gunor, R.H.S. Winterton, A general correlation for flow boiling in tubes and annuli, *Int. J. Heat Mass Transf.* 29 (1986) 351–358, [https://doi.org/10.1016/0017-9310\(86\)90205-X](https://doi.org/10.1016/0017-9310(86)90205-X).
- [51] Z. Liu, R.H.S. Winterton, A general correlation for saturated and subcooled flow boiling in tubes and annuli, based on a nucleate pool boiling equation, *Int. J. Heat Mass Transf.* 34 (1991) 2759–2766, [https://doi.org/10.1016/0017-9310\(91\)90234-6](https://doi.org/10.1016/0017-9310(91)90234-6).

- [52] W. Qu, I. Mudawar, Measurement and prediction of pressure drop in two-phase micro-channel heat sinks, *Int. J. Heat Mass Transf.* 46 (2003) 2737–2753, [https://doi.org/10.1016/S0017-9310\(03\)00044-9](https://doi.org/10.1016/S0017-9310(03)00044-9).
- [53] R. Revellin, S. Lips, P. Neveu, J. Bonjour, A comprehensive non-equilibrium thermodynamic analysis applied to a vapor–liquid two-phase flow of a pure fluid, *Int. J. Multiph. Flow* 42 (2012) 184–193, <https://doi.org/10.1016/j.ijmultiphaseflow.2006.02.0>.
- [54] E.W. Lemmon, L.H. Bell, M.L. Huber, M.O. McLinden, NIST standard reference database 23: reference fluid thermodynamic and transport properties-REFPROP, Version 10.0, National Institute of Standards and Technology, Standard Reference Data Program, Gaithersburg, 2018.
- [55] R.B. Abernethy, J.W. Thompson Jr., Uncertainty in gas turbine measurements, in: Proceedings of the 9th Propulsion conference, 1973, p. 1230, <https://doi.org/10.2514/6.1973-1230>.
- [56] R.J. Moffat, Describing the uncertainties in experimental results, *Exp. Therm. Fluid Sci.* 1 (1988) 3–17, [https://doi.org/10.1016/0894-1777\(88\)90043-X](https://doi.org/10.1016/0894-1777(88)90043-X).
- [57] V. Gnielinski, New equations for heat and mass transfer in turbulent pipe and channel flow, *Int. Chem. Eng.* 16 (1976) 359–368.
- [58] A.P. Colburn, *Trans AIChE* 29 (1933) 174–210.
- [59] H. Hausen, *Heat Transfer in Counterflow, Parallel Flow and Cross Flow*, McGraw-Hill, 1983.
- [60] S.W. Churchill, H. Ozoe, Correlations for laminar forced convection with uniform heating in flow over a plate and in developing and fully developed flow in a tube, *J Heat Transfer* 95 (1973) 78–84, <https://doi.org/10.1115/1.3450009>.
- [61] R. Revellin, V. Dupont, T. Ursenbacher, J.R. Thome, I. Zun, Characterization of diabatic two-phase flows in microchannels: flow parameter results for R-134a in a 0.5mm channel, *Int. J. Multiph. Flow* 32 (2006) 755–774.
- [62] A.A. Arcano, C.B. Tibiriçá, G. Ribatski, Evaluation of flow patterns and elongated bubble characteristics during the flow boiling of halocarbon refrigerants in a micro-scale channel, *Exp. Therm. Fluid Sci.* 34 (2010) 766–775, <https://doi.org/10.1016/j.expthermflusci.2010.01.006>.
- [63] C.L. Ong, J.R. Thome, Macro-to-microchannel transition in two-phase flow: part 1 – Two-phase flow patterns and film thickness measurements, *Exp. Therm. Fluid Sci.* 35 (2011) 37–47, <https://doi.org/10.1016/j.expthermflusci.2010.08.00>.
- [64] Z.Q. Yang, M. Gong, G. Chen, Z. Lin, H. Huang, H. Feng, A new diabatic two phase flow pattern transition model of R600a, *Int. J. Refrig.* 99 (2019) 138–144, <https://doi.org/10.1016/j.ijrefrig.2018.12.025>.
- [65] T.A. Moreira, R.W. Morse, K.M. Dressler, G. Ribatski, A. Berson, Liquid-film thickness and disturbance-wave characterization in a vertical, upward, two-phase annular flow of saturated R245fa inside a rectangular channel, *Int. J. Multiph. Flow* 132 (2020), 103412, <https://doi.org/10.1016/j.ijmultiphaseflow.2020.1034>.
- [66] J.D. Da Silva, *Estudo Teórico-Experimental Da Perda De Pressão Durante a Ebulação Convectiva De Refrigerantes Halogenados No Interior De Microcanais Circulares* PhD Thesis, University of São Paulo, São Carlos, Brazil, 2012.
- [67] W. McAdams, W. Woods, R. Bryan, Vaporization inside horizontal tubes II: benzene-oil mixtures, *Trans. ASME* 64 (1942) 193–200.
- [68] A. Cicchitti, C. Lombardi, M. Silvestri, G. Soldaini, R. Zavattarelli, Two-phase cooling experiments—Pressure drop, heat transfer and burnout measurements, *Energ. Nucl.* 7 (1960) 407–425.
- [69] A.E. Dukler, M. Wicks III, R.G. Cleveland, Frictional pressure drop in two-phase flow: B. An approach through similarity analysis, *AICHE J.* 10 (1964) 44–51, <https://doi.org/10.1002/aic.690100118>.
- [70] D.R.H. Beattie, P.B. Whalley, A simple two-phase frictional pressure drop calculation method, *Int. J. Multiph. Flow* 8 (1982) 83–87, [https://doi.org/10.1016/0301-9322\(82\)90009-X](https://doi.org/10.1016/0301-9322(82)90009-X).
- [71] S. Lin, C.C.K. Kwok, R.Y. Li, Z.H. Chen, Z.Y. Chen, Local frictional pressure drop during vaporization of R-12 through capillary tubes, *Int. J. Multiph. Flow* 17 (1991) 95–102, [https://doi.org/10.1016/0301-9322\(91\)90072-B](https://doi.org/10.1016/0301-9322(91)90072-B).
- [72] F. Garcia, R. Garcia, J.C. Padrino, C. Mata, J.L. Trallero, D.D. Joseph, Power law and composite power law friction factor correlations for laminar and turbulent gas–liquid flow in horizontal pipelines, *Int. J. Multiph. Flow* 29 (2003) 1605–1624, [https://doi.org/10.1016/S0301-9322\(03\)00139-3](https://doi.org/10.1016/S0301-9322(03)00139-3).
- [73] M.M. Awad, Y.S. Muzychka, Effective property models for homogeneous two-phase flows, *Exp. Therm. Fluid Sci.* 33 (2008) 106–113, <https://doi.org/10.1016/j.expthermflusci.2008.07.006>.
- [74] M. Ducoulombier, S. Collasson, J. Bonjour, P. Haberschill, Carbon dioxide flow boiling in a single microchannel-Part I: pressure drops, *Exp. Therm. Fluid Sci.* 35 (2011) 581–596, <https://doi.org/10.1016/j.expthermflusci.2010.12.010>.
- [75] K. Mishima, T. Hibiki, Some characteristics of air-water two-phase flow in small diameter vertical tubes, *Int. J. Multiph. Flow* 22 (1996) 703–712, [https://doi.org/10.1016/0301-9322\(96\)00010-9](https://doi.org/10.1016/0301-9322(96)00010-9).
- [76] S.M. Kim, I. Mudawar, Universal approach to predicting two-phase frictional pressure drop for mini/micro-channel saturated flow boiling, *Int. J. Heat Mass Transf.* 57 (2013) 718–734, <https://doi.org/10.1016/j.ijheatmasstransfer.2012.11.045>.
- [77] F. Nie, S. Yan, H. Wang, C. Zhao, Y. Zhao, M. Gong, A universal correlation for predicting two-phase frictional pressure drop in horizontal tubes based on machine learning, *Int. J. Multiph. Flow* 160 (2023), 104377, <https://doi.org/10.1016/j.ijmultiphaseflow.2022.1043>.
- [78] Y. Xu, X. Fang, A new correlation of two-phase frictional pressure drop for evaporating flow in pipes, *Int. J. Refrig.* 35 (2012) 2039–2050, <https://doi.org/10.1016/j.ijrefrig.2012.06.011>.
- [79] D.F. Semperetegui-Tapia, G. Ribatski, Two-phase frictional pressure drop in horizontal micro-scale channels: experimental data analysis and prediction method development, *Int. J. Refrig.* 79 (2017) 143–163, <https://doi.org/10.1016/j.ijrefrig.2017.03.024>.
- [80] C.B. Tibiriçá, D.M. Rocha, I.L.S. Sueth Jr, G. Bochio, G.K.K. Shimizu, M.C. Barbosa, S. dos Santos Ferreira, A complete set of simple and optimized correlations for microchannel flow boiling and two-phase flow applications, *Appl. Therm. Eng.* 126 (2017) 774–795, <https://doi.org/10.1016/j.applthermaleng.2017.07.1>.
- [81] A. Zhao, Y. Fan, Y. Suzuki, K. Morimoto, Dryout characteristics of low-GWP working fluids at low mass and heat fluxes in a vertical 4mm diameter tube, *Int. J. Heat Mass Transf.* 172 (2021), 121114, <https://doi.org/10.1016/j.ijheatmasstransfer.2021.121>.
- [82] R.W. Morse, T.A. Moreira, J. Chan, K.M. Dressler, G. Ribatski, E.T. Hurlburt, L. L. McCarrol, G.F. Nellis, A. Berson, Critical heat flux and the dryout of liquid film in vertical two-phase annular flow, *Int. J. Heat Mass Transf.* 177 (2021), 121487, <https://doi.org/10.1016/j.ijheatmasstransfer.2021.121>.
- [83] V.E.C. Baptista, T.A. Moreira, G. Ribatski, Liquid-film thickness during flow boiling of pure hydrocarbons and their mixtures, *Exp. Therm. Fluid Sci.* 144 (2023), 110877, <https://doi.org/10.1016/j.expthermflusci.2023.110877>.
- [84] F.T. Kanizawa, C.B. Tibiriçá, G. Ribatski, Heat transfer during convective boiling inside microchannels, *Int. J. Heat Mass Transf.* 93 (2016) 566–583, <https://doi.org/10.1016/j.ijheatmasstransfer.2015.09.083>.
- [85] Z. Shen, D. Yang, H. Xie, X. Nie, W. Liu, S. Wang, Flow and heat transfer characteristics of high-pressure water flowing in a vertical upward smooth tube at low mass flux conditions, *Appl. Therm. Eng.* 102 (2016) 391–401, <https://doi.org/10.1016/j.applthermaleng.2016.03.1>.
- [86] P.A. Kew, K. Cornwell, Correlations for the prediction of boiling heat transfer in small-diameter channels, *Appl. Therm. Eng.* 17 (1997) 705–715, [https://doi.org/10.1016/S1359-4311\(96\)00071-3](https://doi.org/10.1016/S1359-4311(96)00071-3).
- [87] L. Sun, K. Mishima, An evaluation of prediction methods for saturated flow boiling heat transfer in mini-channels, *Int. J. Heat Mass Transf.* 52 (2009) 5323–5329, <https://doi.org/10.1016/j.ijheatmasstransfer.2009.06>.
- [88] D.S. Jung, M. McLinden, R. Radermacher, D. Didion, A study of flow boiling heat transfer with refrigerant mixtures, *Int. J. Heat Mass Transf.* 32 (1989) 1751–1764, [https://doi.org/10.1016/0017-9322\(89\)90057-4](https://doi.org/10.1016/0017-9322(89)90057-4).
- [89] R. Yun, Y. Kim, M.S. Kim, Flow boiling heat transfer of carbon dioxide in horizontal mini tubes, *Int. J. Heat Fluid Flow* 26 (2005) 801–809, <https://doi.org/10.1016/j.ijheatfluidflow.2005.01.00>.
- [90] M. Ozawa, T. Ami, I. Ishihara, H. Umekawa, R. Matsumoto, Y. Tanaka, T. Yamamoto, Y. Ueda, Flow pattern and boiling heat transfer of CO₂ in horizontal small-bore tubes, *Int. J. Multiph. flow* 35 (2009) 699–709, <https://doi.org/10.1016/j.ijmultiphaseflow.2009.04.0>.
- [91] D. Del Col, Flow boiling of halogenated refrigerants at high saturation temperature in a horizontal smooth tube, *Exp. Therm. Fluid Sci.* 34 (2010) 234–245, <https://doi.org/10.1016/j.expthermflusci.2009.10.035>.
- [92] M. Ducoulombier, S. Collasson, J. Bonjour, P. Haberschill, Carbon dioxide flow boiling in a single microchannel-Part II: heat transfer, *Exp. Therm. Fluid Sci.* 35 (2011) 597–611, <https://doi.org/10.1016/j.expthermflusci.2010.12.010>.
- [93] S.M. Kim, I. Mudawar, Universal approach to predicting saturated flow boiling heat transfer in mini/micro-channels-Part II: Two-phase heat transfer coefficient, *Int. J. Heat Mass Transf.* 64 (2013) 1239–1256, <https://doi.org/10.1016/j.ijheatmasstransfer.2013.04.014>.